Supporting Information

Heterometallic Multinuclear Nodes Directing MOF Electronic Behavior

Otega A. Ejegbavwo,[‡a] Anna A. Berseneva,[‡a] Corey R. Martin,[a] Gabrielle A. Leith,[a] Shubham Pandey,[d] Amy J. Brandt,[a] Kyoung Chul Park,[a] Abhijai Mathur,[a] Sharfa Farzandh,[a] Vladislav V. Klepov,[a] Brittany J. Heiser,[a] Mvs Chandrashekhar,[b] Stavros G. Karakalos,[c] Mark D. Smith,[a] Simon R. Phillpot,[d] Sophya Garashchuk,[a] Donna A. Chen,*[a] and Natalia B. Shustova*[a]

[a]*Department of Chemistry and Biochemistry, University of South Carolina, Columbia, South Carolina 29208, United States*
[b]*Department of Electrical Engineering, University of South Carolina, Columbia, South Carolina 29208, United States*
[c]*College of Engineering and Computing, University of South Carolina, Columbia, South Carolina 29208, United States*
[d]*Department of Materials Science and Engineering, University of Florida, Gainesville, Florida 32611, United States*

Table of contents: **page number**

Materials. $Cu(NO_3)_2 \cdot 2.5H_2O$ (98.3%, Mallinckrodt AR), $Cu(OAc)_2 \cdot H_2O$ (>95%, TCI America), $CoCl_2 \cdot 6H_2O$ (>98.0%, TCI America), $Co(OAc)_2 \cdot 4H_2O$ (98%, Alfa Aesar), $Co(NO_3)_2 \cdot 6H_2O$ (99 %, Stem Chemicals Inc.), $Mn(OAc)_2 \cdot 4H_2O$ (99.9%, Alfa Aesar), $MnCl_2 \cdot 4H_2O$ (98%, Alfa Aesar), $FeCl_2 \cdot 4H_2O$ (reagent grade, Ward's Science), $Ni(OAc)_2 \cdot 4H_2O$ (98+%, Alfa Aesar), $NiCl_2 \cdot 6H_2O$ (98%, Alfa Aesar), $Zn(NO_3)_2 \cdot 6H_2O$ (technical grade, Ward's Science), $RhCl_3 \cdot H_2O$ (99.98%, Engelhard Chemicals), 1,3,5-benzenetricarboxylic acid (98%, Alfa Aesar), 5-nitroisophthalic acid (98%, BeanTown Chemical), 2,3,6,7,10,11-hexahydroxytriphenylene (95%, Acros Chemical), *N*,*N*′-dimethylformamide (ACS grade, BDH), methanol (>99.8%, HPLC grade, Fisher Scientific), nitric acid (98%, Alfa Aesar), hydrochloric acid (ACS grade, Oakwood Chemical), acetone (ACS grade, BDH), and ethanol (200 proof, Decon Laboratories, Inc.) were used as received.

Synthesis of monometallic MOFs, $Cu_3(BTC)_2$ (BTC^{3-} = 1,3,5-benzenetricarboxylate),[1] $Zn_3(BTC)_2$,[2] $Cu_5(NIP)_4(OH)_2$,[3] ($Cu_5(NIP)_4$; NIP^{2-} = 5-nitroisophthalate), $Co_9(HHTP)_4$ ($HHTP^{3-}$ = triphenylene-2,3,6,7,10,11-hexaone),[4] and $Cu_3(HHTP)_2$[4] were performed based on the reported procedures. The corresponding material characterization was performed using powder X-ray diffraction (PXRD, Figures S2, S7, S12, and S17), thermogravimetric analysis (TGA, Figures S4 and S20), and Fourier-transform infrared spectroscopy (FTIR, Figures S5, S16, and S21).

Synthesis of $Cu_3(BTC)_2$ Single Crystals

For single crystal preparation of $Cu_3(BTC)_2$, $Cu(NO_3)_2 \cdot 2.5H_2O$ (89.8 mg, 0.386 mmol), H_3BTC (49.2 mg, 0.234 mmol), and *N,N*-dimethylformamide (DMF):H_2O:EtOH solvent mixture (1:1:1, total volume = 6.00 mL) were added to a 20 mL vial and the mixture was sonicated for 5 min. The mixture was heated at 75 °C in an oven for 24 h. After cooling to room temperature, the blue crystals of $Cu_3(BTC)_2$ (96% yield) were collected by filtration and washed thoroughly with DMF (3 × 20 mL). The yield was recorded upon drying in air for 1 h. PXRD studies confirmed the crystallinity of the bulk material (Figure S7).

Synthesis of Heterometallic MOFs

$Cu_{2.5}Co_{0.5}$-HHTP. In a 20 mL vial, powder of $Co_9(HHTP)_4$ (20.0 mg, 11.0 μmol) was added to an aqueous solution of $Cu(OAc)_2$ (0.069 M, 1.00 mL) and stirred for 16 h at 85 °C on a hotplate. The dark powder, obtained in 88% yield, was collected by filtration and washed thoroughly with deionized water (2 × 20 mL) and then with acetone (3 × 20 mL). The yield was recorded upon drying in air for 1 h. PXRD studies were used to confirm crystallinity of bulk material after transmetallation (Figure S2). TGA was used to evaluate stability of the obtained framework and the corresponding TGA plot is shown in Figure S4. The FTIR spectrum is shown in Figure S5. The composition of the prepared sample was estimated based on inductively coupled plasma mass spectrometry (ICP-MS) data; prior to this analysis, the sample was subjected to an extensive washing procedure using the Soxhlet apparatus for seven days with water and acetone solvent mixture.

$Cu_{2.0}Mn_{1.0}$-HHTP. In a 20 mL vial, powder of $Cu_3(HHTP)_2$ (50.0 mg, 60.0 μmol) was added to an aqueous solution of $Mn(OAc)_2$ (0.110 M, 2.00 mL) and stirred for 16 h at 85 °C on a hotplate. The dark blue powder, obtained in 70% yield, was collected by filtration and washed thoroughly with deionized water (2 × 20 mL) and then with acetone (3 × 20 mL). The yield was recorded upon drying in air for 1 h. PXRD studies were used to confirm crystallinity of bulk material after transmetallation (Figure S3). The FTIR spectrum is shown in Figure S5. The composition of the prepared sample was estimated based on ICP-MS data; prior to this analysis, the sample was

subjected to an extensive washing procedure using the Soxhlet apparatus for seven days with water and acetone solvent mixture.

$Cu_{1.5}Ni_{1.5}$-HHTP. In a 20 mL vial, powder of $Cu_3(HHTP)_2$ (50.0 mg, 60.0 μmol) was added to an aqueous solution of $Ni(OAc)_2$ (0.110 M, 2.00 mL) and stirred for 16 h at 85 °C on a hotplate. The dark blue powder, obtained in 78% yield, was collected by filtration and washed thoroughly with deionized water (2 × 20 mL) and then with acetone (3 × 20 mL). The yield was recorded upon drying in air for 1 h. PXRD studies were used to confirm crystallinity of bulk material after transmetallation (Figure S3). The FTIR spectrum is shown in Figure S5. The composition of the prepared sample was estimated based on ICP-MS data; prior to this analysis, the sample was subjected to an extensive washing procedure using the Soxhlet apparatus for seven days with water and acetone solvent mixture.

$Cu_{2.6}Rh_{0.4}$-HHTP. In a 20 mL vial, powder of $Cu_3(HHTP)_2$ (50.0 mg, 60.0 μmol) was added to an aqueous solution of $RhCl_3$ (38.0 mM, 2.00 mL) and stirred for 16 h at 85 °C on a hotplate. The dark powder, obtained in 58% yield, was collected by filtration and washed thoroughly with deionized water (2 × 20 mL) and then with acetone (3 × 20 mL). The yield was recorded upon drying in air for 1 h. PXRD studies were used to confirm crystallinity of bulk material after transmetallation (Figure S3). The FTIR spectrum is shown in Figure S5. The composition of the prepared sample was estimated based on ICP-MS data; prior to this analysis, the sample was subjected to an extensive washing procedure using the Soxhlet apparatus for seven days water and acetone solvent mixture.

$Cu_{3-X}Mn_X(BTC)_2$. The heterometallic MOFs $Cu_{2.8}Mn_{0.2}$-BTC, $Cu_{2.6}Mn_{0.4}$-BTC, and $Cu_{2.4}Mn_{0.6}$-BTC were prepared by heating crystals of $Cu_3(BTC)_2$ (450 mg, 0.744 mmol) in a DMF solution of $MnCl_2$ (0.250 M, 10.0 mL) in a 20 mL vial for 24, 48, and 72 h, respectively, at 90 °C in a preheated oven. The yields for $Cu_{2.8}Mn_{0.2}$-BTC, $Cu_{2.6}Mn_{0.4}$-BTC, and $Cu_{2.4}Mn_{0.6}$-BTC were found to be 81%, 79%, and 77%, respectively. The yields were recorded upon drying in air for 1 h. Before further characterization of the prepared green crystals, a solvent exchange procedure was performed. The heterometallic samples were immersed in ethanol for three days, and ethanol was refreshed twice each day. The prepared crystals of $Cu_{3-X}Mn_X(BTC)_2$ MOFs were suitable for single-crystal X-ray analysis. The detailed description of the data collection and refinement details are given below. Tables S1 and S2 contain the crystallographic refinement data of $Cu_{3-X}Mn_X$-BTC MOFs. The crystallinity of heterometallic samples was confirmed by PXRD (Figure S8). TGA was used to evaluate stability of the obtained framework, and the corresponding TGA plot is shown in Figure S13. The FTIR spectrum is shown in Figure S16. The composition of the prepared samples was estimated based on ICP-MS data; prior to this analysis, the sample was subjected to an extensive washing procedure using the Soxhlet apparatus for seven days with DMF and ethanol solvent mixture.

$Cu_{3-X}Fe_X(BTC)_2$. The heterometallic MOFs $Cu_{2.7}Fe_{0.3}$-BTC, $Cu_{2.6}Fe_{0.4}$-BTC, and $Cu_{2.2}Fe_{0.8}$-BTC were prepared by heating crystals of $Cu_3(BTC)_2$ (450 mg, 0.744 mmol) in a DMF solution of $FeCl_2$ (67.0 mM, 10.0 mL) in a 20 mL vial for 24, 48, and 72 h, respectively, at 90 °C in a preheated oven. The yields for $Cu_{2.7}Fe_{0.3}$-BTC, $Cu_{2.6}Fe_{0.4}$-BTC, and $Cu_{2.2}Fe_{0.8}$-BTC were found to be 79%, 71%, and 65%, respectively. The yields were recorded upon drying in air for 1 h. Before further characterization of the prepared green crystals, a solvent exchange procedure was performed. The

heterometallic samples were immersed in ethanol for three days, and ethanol was refreshed twice each day. The prepared crystals of $Cu_{3-X}Fe_X(BTC)_2$ MOFs were suitable for single-crystal X-ray studies. The detailed description of the data collection and refinement details are given below. Tables S1 and S2 contain the crystallographic refinement data of $Cu_{3-X}Fe_X$-BTC MOFs. The crystallinity of heterometallic samples was confirmed by PXRD (Figure S9). TGA was used to evaluate stability of the obtained framework, and the corresponding TGA plot is shown in Figure S13. The FTIR spectrum is shown in Figure S16. The composition of the prepared samples was estimated based on ICP-MS data; prior to this analysis, the sample was subjected to an extensive washing procedure using the Soxhlet apparatus for seven days with DMF and ethanol solvent mixture.

$Cu_{3-X}Co_X(BTC)_2$. The heterometallic MOFs, $Cu_{2.9}Co_{0.1}$-BTC, $Cu_{2.82}Co_{0.18}$-BTC, and $Cu_{2.79}Co_{0.21}$-BTC, were prepared by heating crystals of $Cu_3(BTC)_2$ (150 mg, 0.248 mmol) in a DMF solution of $Co(NO_3)_2$ (0.100 M, 5.00 mL) in a 20 mL vial for 12, 42, and 72 h, respectively, at 90 °C in a preheated incubator. The yields for $Cu_{2.9}Co_{0.1}$-BTC, $Cu_{2.82}Co_{0.18}$-BTC, and $Cu_{2.79}Co_{0.21}$-BTC were found to be 80%, 77%, and 75%, respectively. The yields were recorded upon drying in air for 1 h. Before further characterization of the prepared green crystals, a solvent exchange procedure was performed. The heterometallic samples were immersed in ethanol for three days, and ethanol was refreshed twice each day. The prepared crystals of $Cu_{3-X}Co_X(BTC)_2$ MOFs were suitable for single-crystal X-ray analysis. The detailed description of the data collection and refinement details are given below. Tables S1 and S2 contain the crystallographic refinement data of $Cu_{3-X}Co_X$-BTC MOFs. The crystallinity of heterometallic samples was confirmed by PXRD (Figure S10). TGA was used to evaluate stability of the obtained framework, and the corresponding TGA plot is shown in Figure S14. The FTIR spectrum is shown in Figure S16. The composition of the prepared samples was estimated based on ICP-MS data; prior to this analysis, the sample was subjected to an extensive washing procedure using the Soxhlet apparatus for seven days with DMF and ethanol solvent mixture.

$Cu_{2.7}Ni_{0.3}$-BTC. In a 20 mL vial, crystals of $Cu_3(BTC)_2$ (300 mg, 0.496 mmol) were heated in a DMF solution of $NiCl_2$ (0.190 M, 5.00 mL) for 74 h at 90 °C in a preheated incubator. The yield of blue-green crystals was found to be 85%. The yield was recorded upon drying in air for 1 h. Before further characterization of the prepared crystals, a solvent exchange procedure was performed. The heterometallic MOF was immersed in ethanol for three days, and ethanol was refreshed twice each day. The crystallinity of heterometallic samples was confirmed by PXRD (Figure S11). TGA was used to evaluate stability of the obtained frameworks, and the corresponding TGA plot is shown in Figure S14. The FTIR spectrum is shown in Figure S16. The composition of the prepared sample was estimated based on ICP-MS data; prior to this analysis, the sample was subjected to an extensive washing procedure using the Soxhlet apparatus for 7 days with DMF and ethanol solvent mixture.

$Cu_{1.6}Zn_{1.4}$-BTC. In a 20 mL vial, crystals of $Zn_3(BTC)_2$ (380 mg, 0.623 mmol) were soaked in an ethanol solution of $Cu(NO_3)_2$ (1.01 M, 5.00 mL) for 24 h at room temperature. The yield of $Cu_{1.6}Zn_{1.4}$-BTC blue crystals was found to be 80% and was recorded upon drying in air for 1 h. Before further characterization of the prepared crystals, a solvent exchange procedure was performed. The heterometallic MOF was immersed in ethanol for three days, and ethanol was refreshed twice each day. The crystallinity of heterometallic samples was confirmed by PXRD

(Figure S12). TGA was used to evaluate stability of the obtained frameworks, and the corresponding TGA plot is shown in Figure S15. The FTIR spectrum is shown in Figure S16. The composition of the prepared sample was estimated based on ICP-MS data; prior to this analysis, the sample was subjected to an extensive washing procedure using the Soxhlet apparatus for seven days with DMF and ethanol solvent mixture.

$Cu_{4.4}Fe_{0.6}$-NIP. In a 20 mL vial, powder of $Cu_5(NIP)_4$ (399 mg, 0.336 mmol) was soaked in a DMF solution of $FeCl_2$ (67.0 mM, 3.00 mL) for 1 h at room temperature. The yield of the green powder was found to be 88% and was recorded upon drying in air for 1 h. Before further characterization of the prepared powder, a solvent exchange procedure was performed. The heterometallic MOF was immersed in methanol for three days and methanol was refreshed twice each day. The crystallinity of heterometallic samples was confirmed by PXRD (Figure S18). TGA was used to evaluate stability of the obtained frameworks, and the corresponding TGA plot is shown in Figure S19. The FTIR spectrum is shown in Figure S21. The composition of the prepared sample was estimated based on ICP-MS data; prior to this analysis, the sample was subjected to an extensive washing procedure using the Soxhlet apparatus for seven days with DMF as the solvent.

$Cu_{4.8}Mn_{0.2}$-NIP. In a 20 mL vial, powder of $Cu_5(NIP)_4$ (399 mg, 0.336 mmol) was soaked in a DMF solution of $MnCl_2$ (0.250 M, 1.50 mL) for 3.5 h at room temperature. The yield of the green powder was found to be 88% and was recorded upon drying in air for 1 h. Before further characterization of the prepared powder, a solvent exchange procedure was performed. The heterometallic MOF was immersed in methanol for three days, and methanol was refreshed twice each day. The crystallinity of heterometallic samples was confirmed by PXRD (Figure S18). TGA was used to evaluate stability of the obtained frameworks, and the corresponding TGA plot is shown in Figure S19. The FTIR spectrum is shown in Figure S21. The composition of the prepared sample was estimated based on ICP-MS data; prior to this analysis, the sample was subjected to an extensive washing procedure using the Soxhlet apparatus for seven days with DMF as the solvent.

$Cu_{4.8}Rh_{0.2}$-NIP. In a 20 mL vial, powder of $Cu_5(NIP)_4$ (377 mg, 0.317 mmol) was soaked in a DMF solution of $RhCl_3$ (39.0 mM, 3.00 mL) and gently stirred for 5 h at 60 °C on a hotplate. The yield of the green powder was found to be 75% and was recorded upon drying in air for 1 h. Before further characterization of the prepared powder, a solvent exchange procedure was performed. The heterometallic MOF was immersed in methanol for three days, and methanol was refreshed twice each day. The crystallinity of heterometallic samples was confirmed by PXRD (Figure S18). TGA was used to evaluate stability of the obtained frameworks, and the corresponding TGA plot is shown in Figure S20. The FTIR spectrum is shown in Figure S21. The composition of the prepared sample was estimated based on ICP-MS data; prior to this analysis, the sample was subjected to an extensive washing procedure using the Soxhlet apparatus for seven days with DMF as the solvent.

X-ray Crystal Structure Determination

$Cu_{2.4}Mn_{0.6}$-BTC, $Cu_{2.4}Fe_{0.6}$-BTC, and $Cu_{1.9}Co_{1.1}$-BTC. X-ray intensity data from blue green octahedra were collected at 100(2) K using a Bruker D8 QUEST diffractometer equipped with a PHOTON-100 CMOS area detector and an Incoatec microfocus source (Mo-Kα radiation, λ =

0.71073 Å). The raw area detector data frames were reduced and corrected for absorption effects using the Bruker APEX3, SAINT+ and SADABS programs.[5,6] Final unit cell parameters were determined by least-squares refinement of large sets of reflections taken from each data set. The structures were solved with SHELXT.[7,8] Subsequent difference Fourier calculations and full-matrix least-squares refinement against F^2 were performed with SHELXL-2016[7,8] using OLEX2.[9]

The heterometallic frameworks are isostructural and crystallize in the cubic system. The pattern of systematic absences in the intensity data was consistent with the space group *Fm*-3*m*, which was verified by structure solutions and refinements. The asymmetric unit of the structures consist of one unique metal site, one axial site modeled as a water oxygen, and $^1/_6$ of one $C_9H_3O_6^{3-}$ ligand with C_{3v} point symmetry. The axial site is disordered over two symmetry-equivalent positions. Metal atom mixing was diagnosed by first setting the unique metal site as 100% copper and then refining the site occupancy factor (*sof*). In all three cases the *sof*(Cu) decreases slightly below 1.0 (0.963(5) for the Mn crystal, 0.974(6) for Fe, and 0.964(5) for Co). Though a small change from full Cu occupancy, these observed *sof*(Cu) deviations from 1.00 are consistent with some site admixture of a lighter atom onto the site. Subsequently the site was refined as a mixed Cu/Mn, Cu/Fe or Cu/Co site with the total site occupancy constrained to sum to one. The site mixing ratios refined to: Cu/Mn = 0.82(3)/0.18(3), Cu/Fe = 0.81(4)/0.19(4), Cu/Co = 0.64(5)/0.36(5). All non-hydrogen atoms were refined with anisotropic displacement parameters. The unique hydrogen atom H3 bonded to carbon C3 was located by Fourier difference synthesis before being placed in a geometrically idealized position and included as a riding atom with *d*(C–H) = 0.95 Å and *U*iso(H) = 1.2*U*eq(C). No hydrogen atom could be located, and none were calculated for the axial water hydrogen atoms. Observed electron density near this split water site suggests some minor substitution by another solvent, likely DMF, but a reasonable disorder model could not be achieved. The structures contain large cavities filled with heavily disordered solvent species which could not be clearly identified or modeled. Trial modeling efforts suggest mostly water. These species were accounted for with Squeeze.[10] Solvent-accessible volumes (SAV) of 11931 Å^3 (Cu/Mn), 11982 Å^3 (Cu/Fe) and 11938 (Cu/Co) were calculated, containing the equivalent of 588 (Cu/Mn), 477 (Cu/Fe), and 703 (Cu/Co) electrons per unit cell. The scattering contribution of this electron density was added to the structure factors computed from the modeled part of the structure during refinement. The reported crystal density and *F.W.* are calculated from the known part of the structure only.

$Cu_{2.3}Mn_{0.7}$-BTC, $Cu_{1.8}Fe_{1.2}$-BTC, and $Cu_{1.1}Co_{1.9}$-BTC. These crystals were isostructural to those described above. Solution and refinement of these compounds were identical as was the identification and treatment of the metal site mixing and cavity guest disorder.
Relevant information: Site mixing ratios and SAV: Cu/Mn: 0.76(3)/0.24(3), 11413 Å^3; Cu/Fe: 0.606(16)/0.394(16), 11414 Å^3, and Cu/Co: 0.36(3)/0.64(3), 12057 Å^3, respectively.

Table S1. X-ray structure refinement data for $Cu_{2.4}Mn_{0.6}$-BTC, $Cu_{2.4}Fe_{0.6}$-BTC, and $Cu_{1.9}Co_{1.1}$-BTC.[a]

compound	**$Cu_{2.4}Mn_{0.6}$-BTC**	**$Cu_{2.4}Fe_{0.6}$-BTC**	**$Cu_{1.9}Co_{1.1}$-BTC**
formula	$C_{36}H_{12}Cu_{4.89}Mn_{1.11}O_{30}$	$C_{36}H_{12}Cu_{4.89}Fe_{1.11}O_{30}$	$C_{36}H_{12}Cu_{3.85}Co_{2.15}O_{30}$
FW	1296.17	1297.14	1295.68
T, K	100(2)	100(2)	100(2)
crystal system	cubic	cubic	cubic
space group	*Fm*-3*m*	*Fm*-3*m*	*Fm*-3*m*
Z	8	8	8
a, Å	26.3140(11)	26.2988(9)	26.2987(11)
b, Å	26.3140(11)	26.2988(9)	26.2987(11)
c, Å	26.3140(11)	26.2988(9)	26.2987(11)
α, °	90	90	90
β, °	90	90	90
γ, °	90	90	90
V, Å^3	18221(2)	18189.0(19)	18189.0(2)
d_{calc}, g/cm^3	0.945	0.947	0.946
μ, mm^{-1}	1.321	1.346	1.318
F(000)	5101.0	5109.0	5102.0
crystal size, mm^3	0.18 × 0.14 × 0.12	0.22 × 0.2 × 0.14	0.2 × 0.14 × 0.1
theta range	4.378 to 56.59	4.38 to 55.008	2.682 to 59.972
index ranges	$-35 \le h \le 35$ $-35 \le k \le 35$ $-35 \le l \le 35$	$-34 \le h \le 26$ $-25 \le k \le 34$ $-27 \le l \le 32$	$-36 \le h \le 35$ $-36 \le k \le 35$ $-36 \le l \le 36$
refl. collected	159093	29719	52661
data/restraints/ parameters	1179/0/40	1096/0/40	1361/0/40
GOF on F^2	1.185	1.234	1.197
largest diff. peak/hole / eÅ^{-3}	0.44/−0.98	0.46/−0.86	0.46/−0.53
R_1/wR_2, $[I \ge 2\sigma(I)]$[b]	0.0404/0.1332	0.0429/0.1487	0.0418/0.1424

[a] Mo-Kα (λ = 0.71073 Å) radiation
[b] $R_1 = \Sigma||F_o|-|F_c||/ \Sigma |F_o|$, $wR_2 = \{\Sigma [w(F_o^2-F_c^2)^2]/ \Sigma [w(F_{o2})_2]\}^{1/2}$

Table S2. X-ray structure refinement data for $Cu_{2.3}Mn_{0.7}$-BTC, $Cu_{1.8}Fe_{1.2}$-BTC, and $Cu_{1.1}Co_{1.9}$-BTC.[a]

compound	**$Cu_{2.3}Mn_{0.7}$-BTC**	**$Cu_{1.8}Fe_{1.2}$-BTC**	**$Cu_{1.1}Co_{1.9}$-BTC**
formula	$C_{36}H_{12}Cu_{4.58}Mn_{1.42}O_{30}$	$C_{36}H_{12}Cu_{3.64}Fe_{2.36}O_{30}$	$C_{36}H_{12}Cu_{2.19}Co_{3.81}O_{30}$
FW	1293.26	1287.43	1295.51
T, K	100(2)	100(2)	100(2)
crystal system	cubic	cubic	cubic
space group	*Fm*-3*m*	*Fm*-3*m*	*Fm*-3*m*
Z	8.00064	8.00064	8.00064
a, Å	26.2845(9)	26.2777(9)	26.3116(5)
b, Å	26.2845(9)	26.2777(9)	26.3116(5)
c, Å	26.2845(9)	26.2777(9)	26.3116(5)
α, °	90	90	90
β, °	90	90	90
γ, °	90	90	90
V, Å^3	18159.3(19)	18145.2(19)	18215.5(10)
d_{calc}, g/cm^3	0.946	0.947	0.945
μ, mm^{-1}	1.294	1.256	1.314
F(000)	5090.0	5079.0	5101.0
crystal size, mm^3	0.1 × 0.08 × 0.06	0.22 × 0.18 × 0.06	0.18 × 0.15 × 0.08
theta range	4.384 to 52.654	4.384 to 52.668	2.68 to 54.978
index ranges	−32 ≤ h ≤ 32 −30 ≤ k ≤ 28 −29 ≤ l ≤ 32	−32 ≤ h ≤ 28, −29 ≤ k ≤ 32 −31 ≤ l ≤ 32	−34 ≤ h ≤ 34 −34 ≤ k ≤ 34 −34 ≤ l ≤ 34
refl. collected	30641	32934	64604
data/restraints/ parameters	988/0/39	988/0/39	1094/0/40
GOF on F^2	1.040	1.094	1.221
largest diff. peak/hole / eÅ^{-3}	0.60/−0.48	0.31/−0.21	0.40/−0.50
R_1/wR_2, $[I \geq 2\sigma(I)]^b$	0.0399/0.1005	0.0224/0.0597	0.0427/0.1376

[a] Mo-Kα (λ = 0.71073 Å) radiation
[b] $R_1 = \Sigma||F_o|-|F_c||/ \Sigma |F_o|$, $wR_2 = \{\Sigma [w(F_o^2-F_c^2)^2]/ \Sigma [w(F_{o2})_2]\}^{1/2}$

Table S3. Unit cell parameter and selected bond distances in $Cu_3(BTC)_2$, $Cu_{2.4}Mn_{0.6}$-BTC, $Cu_{2.4}Fe_{0.6}$-BTC, and $Cu_{1.9}Co_{1.1}$-BTC (Figure S6) at 100 K.

compound	**$Cu_3(BTC)_2$**	**$Cu_{2.4}Mn_{0.6}$-BTC**	**$Cu_{2.4}Fe_{0.6}$-BTC**	**$Cu_{1.9}Co_{1.1}$-BTC**
a, Å	26.3008(9)	26.3140(11)	26.2988(9)	26.2987(11)
d(Cu1–Cu1), Å	2.6593(11)	2.6580(9)	2.6597(12)	2.6579(8)
d(Cu1–O1), Å	1.956(2)	1.9584(17)	1.957(2)	1.9591(16)
d(Cu1–O3), Å	2.134(5)	2.138(5)	2.140(6)	2.147(4)
d(O1–C1), Å	1.256(3)	1.255(2)	1.257(3)	1.253(2)
d(C1–C2), Å	1.511(6)	1.508(4)	1.508(6)	1.504(4)
d(C2–C3), Å	1.390(3)	1.389(2)	1.391(3)	1.394(2)

Table S4. Unit cell parameter and selected bond distances in $Cu_3(BTC)_2$, $Cu_{2.3}Mn_{0.7}$-BTC, $Cu_{1.8}Fe_{1.2}$-BTC, and $Cu_{1.1}Co_{1.9}$-BTC (Figure S6) at 100 K.

compound	**$Cu_3(BTC)_2$**	**$Cu_{2.3}Mn_{0.7}$-BTC**	**$Cu_{1.8}Fe_{1.2}$-BTC**	**$Cu_{1.1}Co_{1.9}$-BTC**
a, Å	26.3008(9)	26.2845(9)	26.2777(9)	26.3116(5)
d(Cu1–Cu1), Å	2.6593(11)	2.6320(12)	2.6381(6)	2.6588(12)
d(Cu1–O1), Å	1.956(2)	1.948(2)	1.9505(10)	1.958(2)
d(Cu1–O3), Å	2.134(5)	2.183(6)	2.179(3)	2.145(6)
d(O1–C1), Å	1.256(3)	1.268(3)	1.2636(13)	1.257(3)
d(C1–C2), Å	1.511(6)	1.478(5)	1.483(3)	1.505(5)
d(C2–C3), Å	1.390(3)	1.390(3)	1.3897(13)	1.391(3)

Topological Analysis and Voronoi-Dirichlet Tessellation for $Co_9(HHTP)_4$, $Cu_3(BTC)_2$, and $Cu_5(NIP)_4$

Topology was determined using the ADS program integrated in the ToposPro software package.[11,12] The crystal structures were simplified using an established procedure.[13] The resulting nets were classified using the ADS program and the topological database provided with the Topos software. Dirichlet program was employed for Voronoi–Dirichlet polyhedra construction and solid angle evaluation.

Thermogravimetric Analysis of $Cu_{3-X}M'_X(HHTP)_2$, $Cu_{3-X}M'_X(BTC)_2$, and $Cu_{5-X}M'_X(NIP)_4$

The thermal stability of the $Cu_{3-X}M'_X(BTC)_2$ MOFs (where M′ = Mn, Fe, Co, and Ni; Figures S13 and S14) and $Cu_{3-X}Zn_XBTC$ (Figure S15) was studied by TGA. The TGA plots (Figures S13–S15) demonstrate the rapid loss of solvent molecules at 28−150 °C. The observed weight loss (≤ 40 wt%) in $Cu_{3-X}M'_X(BTC)_2$ (where M′ = Mn, Fe, Co, Ni, Zn) systems at this temperature range can be attributed to removal of non-coordinated solvents (e.g., DMF, ethanol, and/or water), which is in good correlation with the residual electron density calculated from the single-crystal X-ray data. The thermal stability studies of the $Cu_{5-X}M'_X(NIP)_4$ MOFs (where M′ = Mn, Fe, and Rh) demonstrate the loss of solvent molecules at 28−100 °C (Figures S19 and S20). Overall, the described $Cu_{3-X}M'_X(BTC)_2$ and $Cu_{5-X}M'_X(NIP)_4$ MOFs maintain thermal stability up to 250 °C. TGA plots of $Cu_{3-X}Co_X(HHTP)_2$ MOFs demonstrate that stability is maintained upon incorporation of the second metal. The weight loss (≤ 35 wt%) occurring in a temperature range of 28−200 °C demonstrates the removal of solvent molecules followed by a gradual decomposition of MOF (Figure S4).

X-ray Photoelectron Spectroscopy (XPS) Studies of $Cu_{3-X}M'_X(HHTP)_2$, $Cu_{3-X}M'_X(BTC)_2$, and $Cu_{5-X}M'_X(NIP)_4$

The X-ray photoelectron spectroscopic (XPS) studies were employed to investigate the oxidation state of the metals incorporated into the studied heterometallic MOF structures. Furthermore, employing the XPS technique also provides a non-destructive analytical route through which the electronic properties of the MOFs can be studied by monitoring the population of the density of states (DOS) near the Fermi energy level.[2] Accounting for the significant contribution from the adventitious carbon binding energies, all spectra were calibrated according to the position of the 284.8 eV peak.[14,15] To establish the purity of the samples, survey scans were collected for each sample followed by the relevant regions, including C(1s), O(1s), Cu(2p), Cu(LMM), M′(2p) for M′ = Mn, Fe, Co, Ni, and Zn, and M′(3d) for M′ = Rh. The prepared powder of $Cu_{3-X}M'_X(HHTP)_2$, $Cu_{3-X}M'_X(BTC)_2$, and $Cu_{5-X}M'_X(NIP)_4$ MOFs were evacuated under appropriate conditions (Table 1 in the main text) under the Schlenk line to remove residual solvent in the pores. Immediately after heating, samples were first refilled with nitrogen and then transported to the XPS facility in closed vials to minimize contact with moisture in the atmosphere. The samples were then loaded into vacuum chamber and evacuated overnight to ensure removal of residual water absorbed during the transfer process.

Determination of valence band onset. For comparing the valence band regions of $Cu_{3-X}M'_X(HHTP)_2$, $Cu_{3-X}M'_X(BTC)_2$, and $Cu_{5-X}M'_X(NIP)_4$ MOFs, we determined the valence band onset.[16] Valence band onset was calculated as the binding energy at the intersection of a line at near 0 intensity, provided by modelling the baseline signal, and a tangent line along the maximum rapid change in intensity. A linear fitting was applied for both lines i.e., baseline and

tangent, using linear regression. Standard errors for linear regression coefficients, intercept and slope, were determined, and then converted to valence band onset standard error using the propagation of uncertainty method. The standard error from this approximation can be found in Table S6.

Assignment of Cu oxidation states. Regarding the assignment of the Cu oxidation states in both the pure monometallic and heterometallic MOFs, the Cu($2p_{3/2}$) peaks around 933.0 and 934.7 eV attributed to Cu^{1+} and Cu^{2+}, respectively, were evaluated. These binding energies are consistent with those that have been reported in the literature for Cu^{1+} and Cu^{2+} complexes.[2] Since the Cu($2p_{3/2}$) binding energy is not significantly different for Cu^{1+} and Cu^0, the Cu(LMM) Auger region was used to distinguish these two oxidation states.[17] The Cu(LMM) peak has a distinctly different peak shape for metallic Cu vs. Cu^{1+} or Cu^{2+}. Specifically, an intense, sharp peak at 568 eV and a smaller peak at 565 eV are observed for metallic Cu, whereas a single broad peak around 572 eV is observed for the Cu ions.[2,18,19] A more detailed discussion of the assignment of Cu oxidation states in the $Cu_3(BTC)_2$ MOF can be found in our previous XPS studies of $Cu_3(BTC)_2$.[2] The Cu($2p_{1/2}$) was not typically collected since it required additional X-ray exposure time, which is known to change Cu oxidation states; moreover, the splitting between the ($2p_{3/2}$) and ($2p_{1/2}$) states remained fixed at 19.9 eV, regardless of whether the Cu in MOF was predominantly Cu^{1+} or Cu^{2+}. In conclusion, the oxidation state of Cu in $Cu_{3-X}M'_X(HHTP)_2$ and $Cu_{3-X}M'_X(BTC)_2$ is +1 and +2, respectively. In contrast, the $Cu_{5-X}M'_X(NIP)_4$ system showed a dominance of Cu in the +2 oxidation state.

Assignment of M′ oxidation state. The M′(2p) for M′ = Mn, Fe, Co, Ni, and Zn, and M′(3d) for M′ = Rh regions were considered in order to determine the oxidation state of M′ in $Cu_{3-X}M'_X(HHTP)_2$, $Cu_{3-X}M'_X(BTC)_2$, and $Cu_{5-X}M'_X(NIP)_4$ MOFs. Oxidation state alignment was performed through comparison of binding energies of the peaks in the listed regions with those that have been reported in the literature for complexes and metal salts with known oxidation states. For instance, the XPS results of the Rh-containing MOFs across the studied systems show a peak at 310.0 eV in the Rh($3d_{5/2}$) region, which corresponds to Rh in the +3 oxidation state.[20]The assignment of Rh^{3+} in the mononuclear $Cu_{2.6}Rh_{0.4}$-HHTP and pentanuclear $Cu_{4.8}Rh_{0.2}$-NIP MOFs is consistent with literature reports of Rh^{3+} in $RhCl_3$ metal salt and other Rh(III) complexes.[20,21] In conclusion, the oxidation state of Mn, Co, Ni, Zn, and Rh in the studied $Cu_{3-X}M'_X(HHTP)_2$, $Cu_{3-X}M'_X(BTC)_2$, and $Cu_{5-X}M'_X(NIP)_4$ MOFs is +2, +2, +2, +2, and +3, respectively, the oxidation state of Fe is +3 in $Cu_{3-X}Fe_X(BTC)_2$.[20–34]

Statistical Description of Conductivity Values for $Cu_{3-X}M'_X(BTC)_2$

The differences in conductivity values were analyzed using descriptive statistics by an analysis of variance (ANOVA) test[35–37] integrated into the MATLAB software. An ANOVA test is applied to determine if the means of each group are statistically different within each group. In our calculations, we used three groups: conductivity values of $Cu_{3-X}Co_X(BTC)_2$, $Cu_{3-X}Fe_X(BTC)_2$, and $Cu_{3-X}Mn_X(BTC)_2$, with five data points per heterometallic sample. It was found that the conductivity values were statistically different within the metal percentage populations of $Cu_{3-X}Co_X(BTC)_2$ (p-value = 3.9×10^{-28}) and $Cu_{3-X}Mn_X(BTC)_2$ (p-value = 7.8×10^{-17}), rejecting the null hypothesis (null hypothesis = all values are statistically the same).[38,39] However, for $Cu_{3-X}Fe_X(BTC)_2$, the null hypothesis failed to be rejected due to a p-value of 0.77 for the conductivity values of $Cu_{2.7}Fe_{0.3}$-BTC within the $Cu_{3-X}Fe_X(BTC)_2$ group.

Physical Measurements

Single-crystal X-ray diffraction studies of the MOF samples were done on a Bruker AXS D8 Advance diffractometer using a Mo-Kα (λ = 0.71073 Å) operating at a voltage of 40 kV and a current of 40 mA. PXRD patterns were recorded on a Rigaku Miniflex II diffractometer using Cu-Kα (λ = 1.5406 Å) radiation with accelerating voltage and current of 30 kV and 15 mA, respectively. TGA was performed on a SDT Q600 Thermogravimetric Analyzer using an alumina boat as a sample holder at a heating rate of 5 °C/min. ICP-MS analysis was conducted using a Finnigan ELEMENT XR double focusing magnetic sector field inductively coupled plasma-mass spectrometer with Ir and/or Rh as internal standards. A Micromist U-series nebulizer (0.2 ml/min, GE, Australia), quartz torch, and injector (Thermo Fisher Scientific, USA) were used for sample introduction. Sample gas flow was 1.08 mL/min and the forwarding power was 1250 W. The samples were digested in Teflon vessels with nitric and hydrochloric acids and then heated at 180 °C for 4 h. XPS measurements were performed using a Kratos AXIS Ultra DLD XPS system with a monochromatic Al Kα source operated at 15 keV and 150 W and a hemispherical energy analyzer. Samples were placed in small powder pockets on the holder and analysis was performed at a pressure below 1×10^{-9} mbar. High-resolution core level spectra were measured with a pass energy of 40 eV, and analysis of the data was carried out using XPSPEAK41 software. A charge neutralizer was used to compensate for sample charging by bombarding the sample with low-energy electrons; electrons are generated by a hot filament, and the trajectories of the electrons toward the sample are by controlled electric and magnetic fields. Diffuse reflectance spectra were collected on an Ocean Optics JAZ spectrometer or a PerkinElmer Lambda 850. For the JAZ spectrometer, an Ocean Optics ISP-REF integrating sphere was connected to the spectrometer using a 450 μm SMA fiber optic cable. Samples were loaded in an 8.0 mm quartz sample cell or pressed between quartz microscope slides, which was referenced to a Spectralon standard. The Tauc analysis was performed using diffuse reflectance data with an assumption of direct band-gap transitions.[40] A linear fitting was applied for the Tauc plot and the standard error from this approximation can be found in Table S8. The conductivity measurements on MOF pressed pellets were performed using a two-probe home-built *in-situ* pressed pellet device[41] connected to a sourcemeter (Keithley Instruments GmbH, Germering, Germany, model 263A). For sample preparation, MOF was initially evacuated to remove solvent molecules (details can be found in Table 1 in main text) and then stored under nitrogen. The MOF powder (10 mg) was quickly transferred using a spatula to a quartz tube resting on one of the stainless steel rods of the home-built device.[41] Next, the second stainless steel rod was quickly placed on top of the powder and the pellet was pressed between the rods. The diameter of the resulting pellet is the same as the inner diameter of the quartz tube (d = 2 mm). The thickness of the pellets was kept consistent (l = 1 mm) by using the same amount of material. After forming a small pellet, the stainless-steel rods were connected to the sourcemeter using alligator clips to perform conductivity measurements. For all measurements, the number of power line cycles (NPLC) was set to 5 with a delay of 1 ms. The electrical conductivity of the prepared pellets was calculated by fitting the obtained linear I−V curves using Ohm's law. The standard error can be found in Table S10.

Theoretical Calculation Methods

Density functional theory (DFT) calculations were performed using the Vienna *ab initio* simulation package (VASP)[42,43] with plane wave basis sets. Projector-augmented wave (PAW)[44,45] pseudopotentials were employed, with the H $1s^1$, C $2s^22p^2$, O $2s^22p^4$, Mn $3p^63d^64s^1$, Fe $3p^63d^74s^1$, Co $3p^63d^84s^1$, Ni $3p^63d^94s^1$, Cu $3p^63d^{10}4s^1$, and Zn $3p^63d^{10}4s^2$ treated explicitly. As a truncated model for the calculations, $Cu_2(OAc)_4$ and $CuM'(OAc)_4$ clusters (where M′ = Co, Ni, Mn, Fe, and Zn) were chosen (Figure S34). The geometries were optimized using the GGA-PBE[46] exchange correlation functionals. The van der Waals interactions were taken into account using the dispersion correction formula in the PBE-D3 functionals by Grimme et al[47] with Becke-Johnson Damping. Additionally, an on-site Coulomb interaction was added to the Co-, Ni-, Mn-, Fe-, Zn-, and Cu-*d* electrons to better describe the strong correlation of these electrons, within the DFT+U formalism.[48] Based on previous studies on doping in Cu_2O,[49] a U-J value of 4.0 eV was used. The plane-wave energy cutoff was set to 520 eV and spin-polarized calculations were performed at the Γ-only **k**-point. Anti-ferromagnetic magnetic ordering of the two metal atoms was found in the ground state for all cases. Structural optimization was performed until the forces on each ion was less than 25 meV/Å using 0.1 meV as the energy tolerance criteria for the electronic step. Gaussian smearing with a width of 0.05 eV was applied to all optimizations. A conjugate-gradient algorithm[50,51] was used to relax all of the ions. The calculations were performed on secondary building units (SBUs) isolated in a cubic box of size 30 Å. The band gaps and partial DOS were calculated by single point calculations using the hybrid HSE06 (25% exact exchange) method[52,53] following the geometry optimizations. The exact exchange for $CuMn(OAc)_4$ cluster was adjusted to 30%, from the standard 25% used for all other calculations, to fit its band gap to experimental trend in this work. This technique of exact exchange modulation for transition metal based systems is well-established in previous reports.[54,55] GGA+U derived wavefunctions were kept constant to perform the HSE calculations.

It was demonstrated that 50% substitution of copper with cobalt, nickel, manganese, and iron in $Cu_2(OAc)_4$ decreases the band gap from 3.86 eV to 3.32 eV, 3.50 eV, 3.65 eV, and 3.70 eV respectively. The partial DOS suggests that this decrease in band gap is associated with changes in electronic structure near the Fermi level. The highest occupied molecular orbital (HOMO) initially was dominated by O-2*p* orbitals in the pristine $Cu_2(OAc)_4$ and after substitution of 50% of copper with M′ (M′ = Co, Ni, Mn, or Fe) was dominated by Co-3*d*, Ni-3*d*, Mn-3*d*, and Fe-3*d* orbitals. Whereas, the lowest unoccupied molecular orbital (LUMO) remained dominated by Cu-3*d* orbitals despite substitution. Substitution of copper with zinc however did not significantly alter the electronic structure and the band gap remained nearly the same. The Zn-3*d* orbitals lie deep inside the occupied bands and the band edges were still dominated by O-2*p* and Cu-3*d* orbitals. These results indicate that cobalt substitution decreases the band gap of $Cu_2(OAc)_4$ cluster the most, followed by nickel, manganese, and iron; while zinc does not affect the band gap.

Theoretical examination of the property–metal node composition of the bimetallic MOFs is based on electronic structure calculations for the molecular cluster $Cu_2(OBn)_4$ and $CuM'(OBn)_4$ (OBn^- = benzoate; M′ = Co, Ni, Mn, Fe, and Zn). Use of these truncated models of the bimetallic MOFs facilitates control of the spin states in these structures. The calculations have been performed using several electronic structure packages: Q-Chem 5.2, Spartan18, and IQmol molecular viewer.[56,57] The electronic structure method used is the unrestricted DFT,[58] specifically the most extensively used functionals were the B3LYP[59,60] and ω-B97X-V.[61] They were both paired with basis m6-31G* that is the 'modified' 6-31G* with an improved representation of the *d*-electrons for first-row transition metals and compared to the results for other bases of the 6-31G

family.[62] The Grimme's dispersion has been invoked[63] and the electron excitations analysis is based on the time-dependent density functional theory (TDDFT)[64] using the Tamm–Dancoff approximation (TDA)[65] or using the random phase approximation (RPA) instead of the TDA.

The molecular geometry has been optimized at the B3LYP/m631-G* level of theory since B3LYP is an accurate method for the geometry optimization of a wide variety of molecular structures including those with metals e.g., MOFs.[66,67] The molecular cluster model is constructed as truncations of binuclear MOF structures of $Cu_3(BTC)_2$ after assessment of the single crystal X-ray data. We have considered the binuclear monometallic $Cu_2(OBn)_4$ and bimetallic $CuM'(OBn)_4$ clusters to be accurate representations of the truncated MOF systems. The main electronic structure method has been selected after considering and testing several density functionals: B3LYP, CAM-B3LYP, LRC-ωPBEh, revM06-L, ω-B97X-D, and ω-B97X-V,[68–70] with and without the D3 dispersion correction. The B3LYP-D3 and ω-B97X-V functionals gave the best agreement of lowest electron excitation of the cluster, i.e., TDDFT 'corrected' HOMO–LUMO gap, with experimentally M′–property established correlation. In the analysis of the electron excitations, we have used the ω-B97X-V functional, as it is known as a method with good accuracy for transition metals. The ω-B97X-V functional was paired with 6-31G, 6-31G*, m6-31G*, 6-31+G*, 6-31+G**, and 6-31++G** bases that yielded marginal changes in the electron excitations of about 0.02–0.13 eV (0.8–6.9%). Based on the literature,[20,67,71] and despite the limitation of the cluster representation of the metal node, that is a 52-atom truncation based on the MOF SBU, we expect that the electronic structure trend on the node composition is reasonably captured by the selected theoretical method. For $Cu_2(OBn)_4$ and $CuM'(OBn)_4$ all possible spin states were considered. To facilitate convergence of the pure spin state, we have used an initial estimation of the wavefunction with 10% of the LUMO and Geometric Direct Minimization method of self-consistent-field convergence (option METSCF = 20). While the high spin (HS) configuration is more energetically favorable for M′ = Co, Ni, Fe, and Zn, for $CuMn(OBn)_4$ the energy difference between HS ($CuMn(OBn)_4$ septet) and low spin (LS, $CuMn(OBn)_4$ quintet) state for Mn-based cluster is rather small (0.007 eV) and LS configuration has lower energy. Since the transition metals can exhibit multiple spin states, in the case of Mn-based cluster, both LS and HS states have been included in the electron excitation analysis.

Within the cluster code calculations, we have estimated the lowest excitation corresponding to the cluster, i.e., TDDFT 'corrected' HOMO–LUMO gap. The results are provided in Table S14. The trend for the lowest electron excitation among metals is the following Co < Ni< Mn < Fe < Cu < Zn for the clusters with the lowest energy. Comparison of LS and HS Mn-based cluster revealed a drastic difference in excitation energy (Table S14). The difference can correspond to different electron transitions, in the case of $CuMn(OBn)_4$ quintet, metal-to-ligand charge transfer (MLCT) takes place and for $CuMn(OBn)_4$ septet, ligand-to-metal charge transfer (LMCT) occurs. The established correlation is in good agreement with VASP calculations and the experimental results from conductivity measurements, VB edge, and optical data.

In order to determine the charge on Cu and M′ in $Cu_2(OBn)_4$ and $CuM'(OBn)_4$ clusters, Bader charge and atomic dipole-corrected-Hishfeld-atomic charge analysis were performed (Table S13) on the optimized geometries with B3LYP-D3/m6-31G* and ω-B97X-V/6-31G* level of theory in the Multiwfn package.[72]

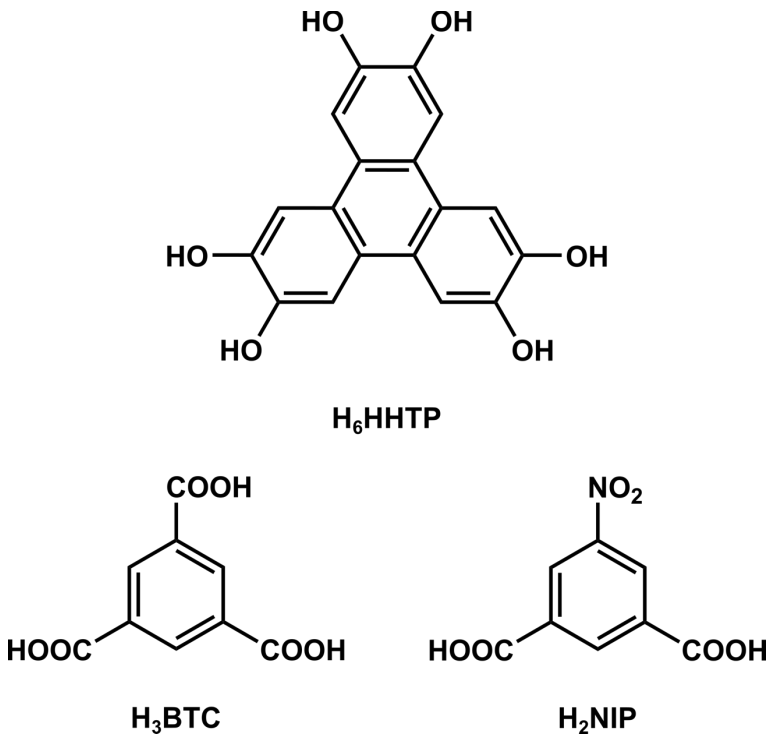

Figure S1. The H_6HHTP, H_3BTC, and H_2NIP linkers used for preparation of MOFs.

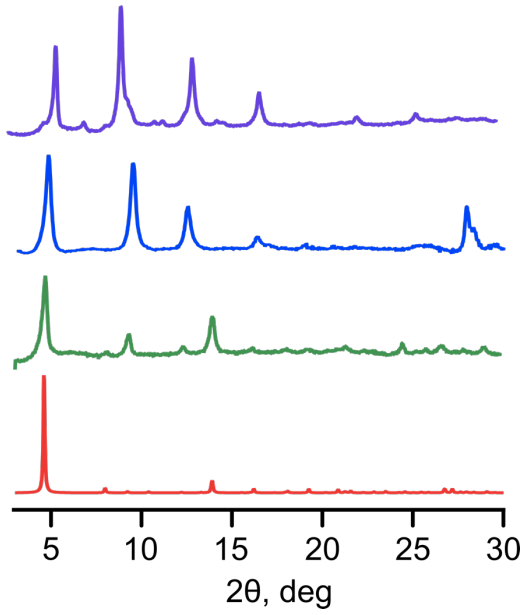

Figure S2. PXRD patterns of simulated $Co_9(HHTP)_4$ (red), experimental $Co_9(HHTP)_4$ (green), experimental $Cu_{2.5}Co_{0.5}$-HHTP (blue), and experimental $Cu_3(HHTP)_2$ (purple).

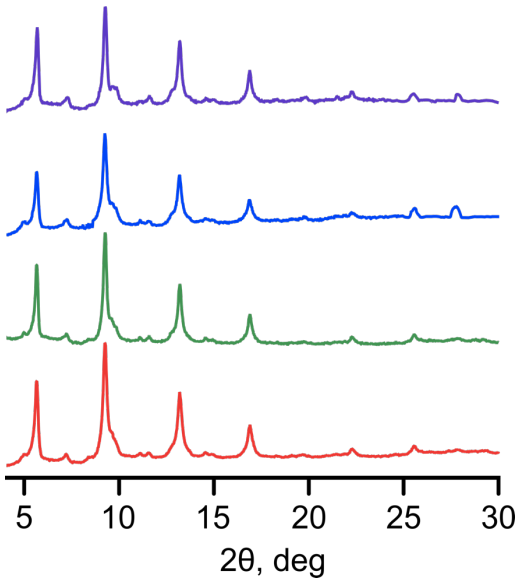

Figure S3. Experimental PXRD patterns of $Cu_3(HHTP)_2$ (red), $Cu_{2.0}Mn_{1.0}$-HHTP (green), $Cu_{1.5}Ni_{1.5}$-HHTP (blue), and $Cu_{2.6}Rh_{0.4}$-HHTP (purple).

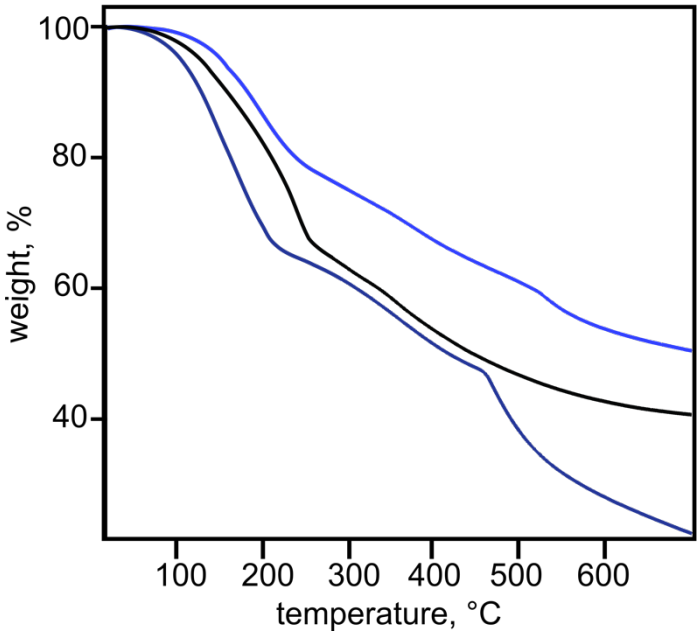

Figure S4. TGA plots of $Co_9(HHTP)_4$ (light blue), $Cu_3(HHTP)_2$ (black), and $Cu_{2.5}Co_{0.5}$-HHTP (dark blue).

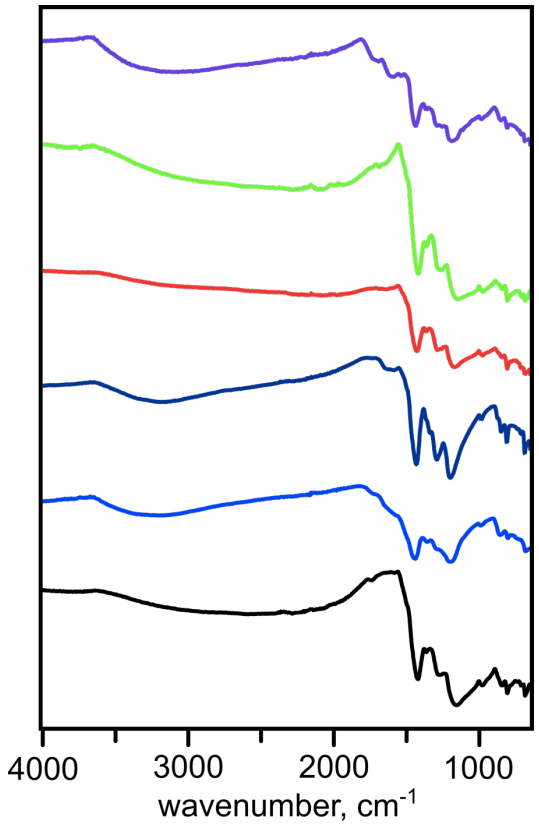

Figure S5. FTIR spectra of: $Cu_3(HHTP)_2$ (black), $Co_9(HHTP)_4$ (blue), $Cu_{2.5}Co_{0.5}$-HHTP (dark blue), $Cu_{2.0}Mn_{1.0}$-HHTP (red), $Cu_{1.5}Ni_{1.5}$-HHTP (light green), and $Cu_{2.6}Rh_{0.4}$-HHTP (purple).

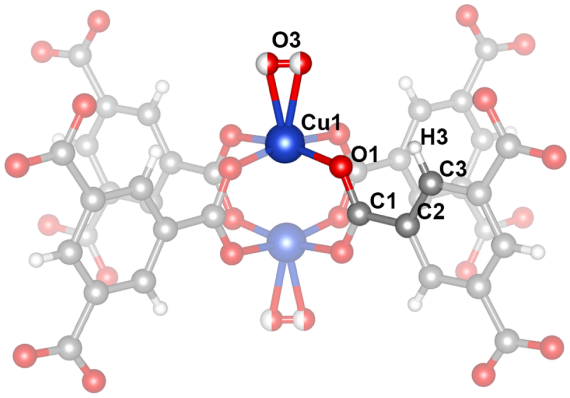

Figure S6. SBU of $Cu_3(BTC)_2$ with labeled atoms. Blue, red, gray, and white spheres represent Cu, O, C, and H atoms, respectively. The O3 atom is disordered over two positions with a 1 to 1 occupancy.

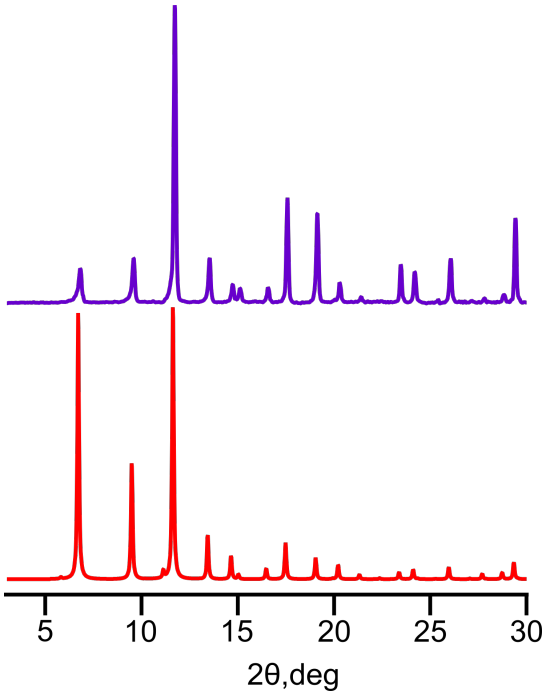

Figure S7. PXRD patterns of $Cu_3(BTC)_2$: simulated (red) and experimental (violet).

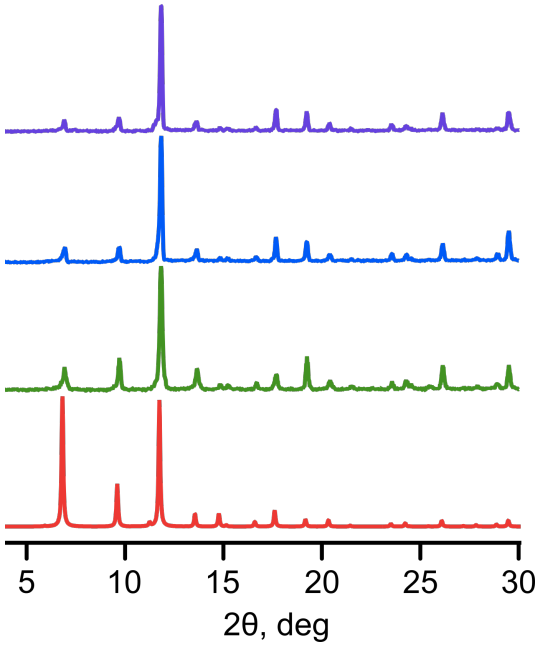

Figure S8. PXRD patterns of simulated $Cu_{2.8}Mn_{0.2}$-BTC (red), experimental $Cu_{2.8}Mn_{0.2}$-BTC (green), experimental $Cu_{2.6}Mn_{0.4}$-BTC (blue), and experimental $Cu_{2.4}Mn_{0.6}$-BTC (purple).

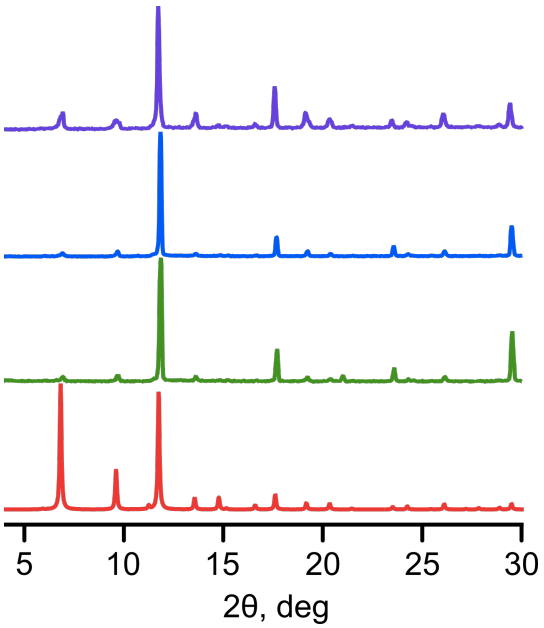

Figure S9. PXRD patterns of simulated $Cu_{2.7}Fe_{0.3}$-BTC (red), experimental $Cu_{2.7}Fe_{0.3}$-BTC (green), experimental $Cu_{2.6}Fe_{0.4}$-BTC (blue), and experimental $Cu_{2.2}Fe_{0.8}$-BTC (purple).

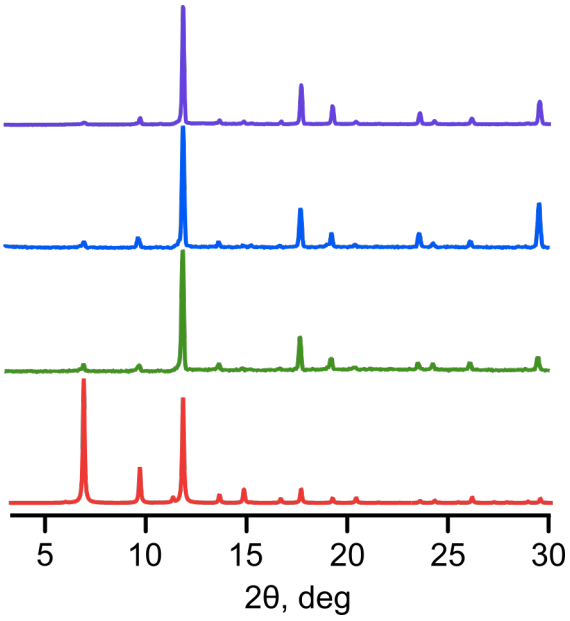

Figure S10. PXRD patterns of simulated $Cu_{2.79}Co_{0.21}$-BTC (red), experimental $Cu_{2.9}Co_{0.1}$-BTC (green), experimental $Cu_{2.82}Co_{0.18}$-BTC (blue), and experimental $Cu_{2.79}Co_{0.21}$-BTC (purple).

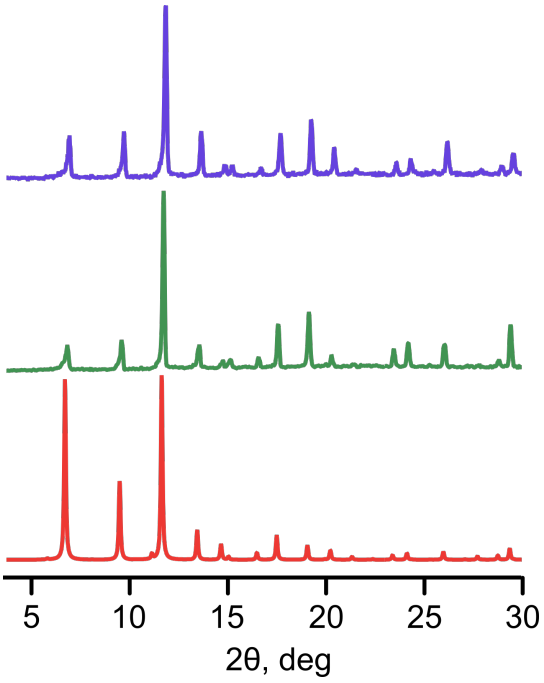

Figure S11. PXRD patterns of simulated $Cu_3(BTC)_2$ (red), experimental $Cu_3(BTC)_2$ (green), and experimental $Cu_{2.7}Ni_{0.3}$-BTC (purple).

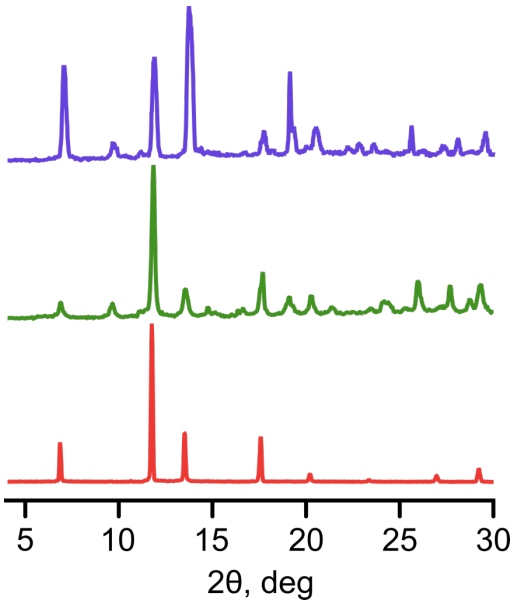

Figure S12. PXRD patterns of simulated $Zn_3(BTC)_2$ (red), experimental $Zn_3(BTC)_2$ (green), and experimental $Cu_{1.6}Zn_{1.4}$-BTC (purple).

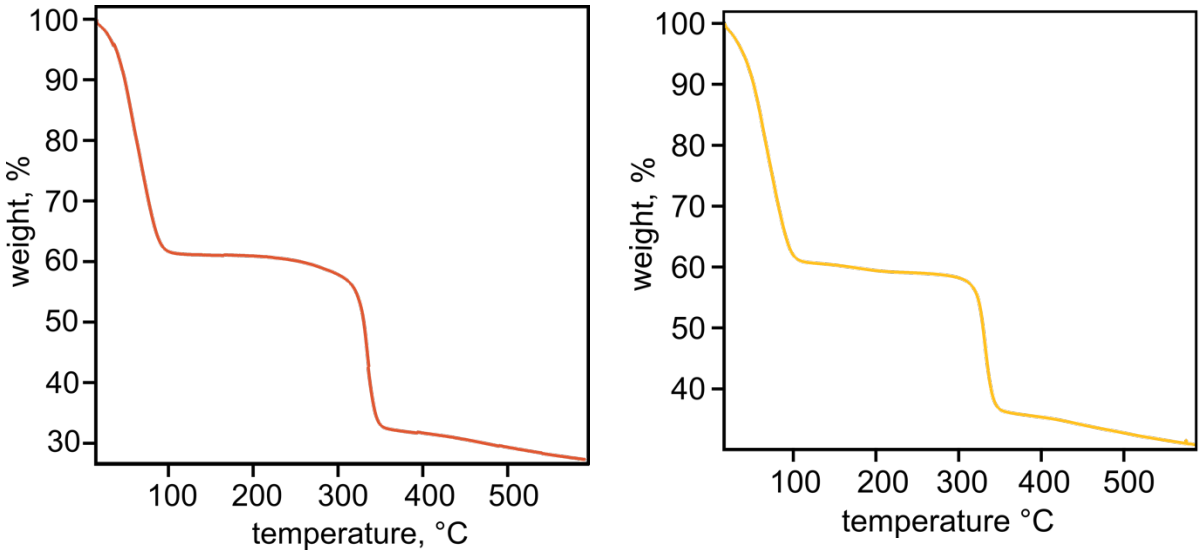

Figure S13. TGA plots of (*left*) $Cu_{2.4}Mn_{0.6}$-BTC and (*right*) $Cu_{2.2}Fe_{0.8}$-BTC.

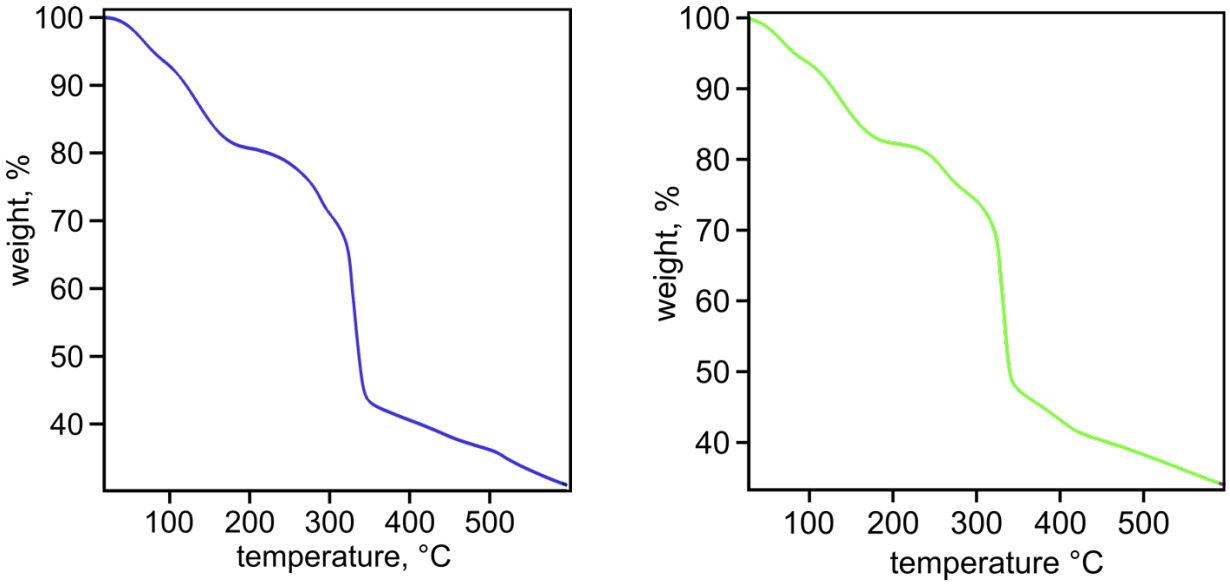

Figure S14. TGA plots of (*left*) $Cu_{2.79}Co_{0.21}$-BTC and (*right*) $Cu_{2.7}Ni_{0.3}$-BTC.

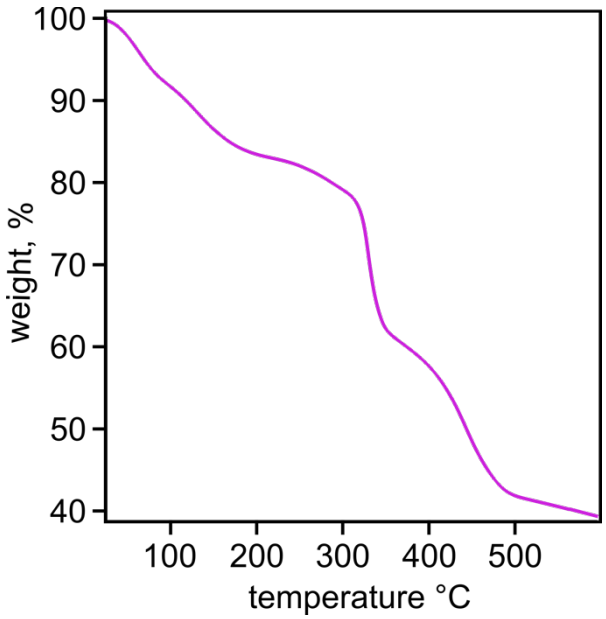

Figure S15. TGA plot of $Cu_{1.6}Zn_{1.4}$-BTC.

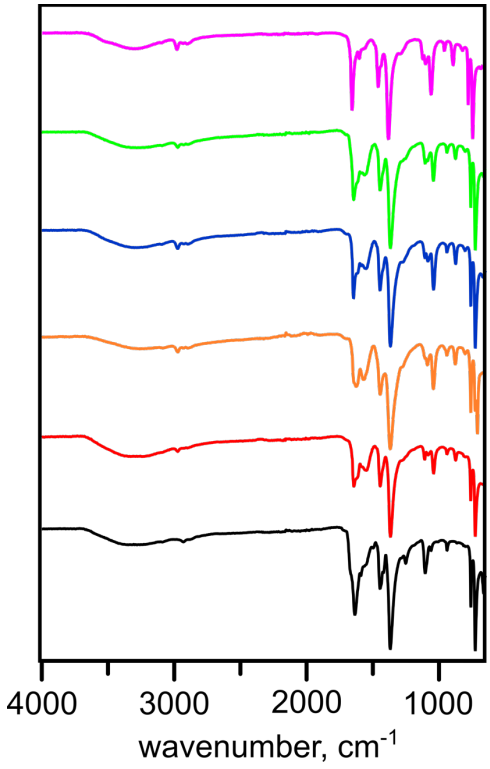

Figure S16. FTIR spectra of $Cu_3(BTC)_2$ (black), $Cu_{2.4}Mn_{0.6}$-BTC (red), $Cu_{2.2}Fe_{0.8}$-BTC (orange), $Cu_{2.79}Co_{0.21}$-BTC (blue), $Cu_{2.7}Ni_{0.3}$-BTC (green), and $Cu_{1.6}Zn_{1.4}$-BTC (pink).

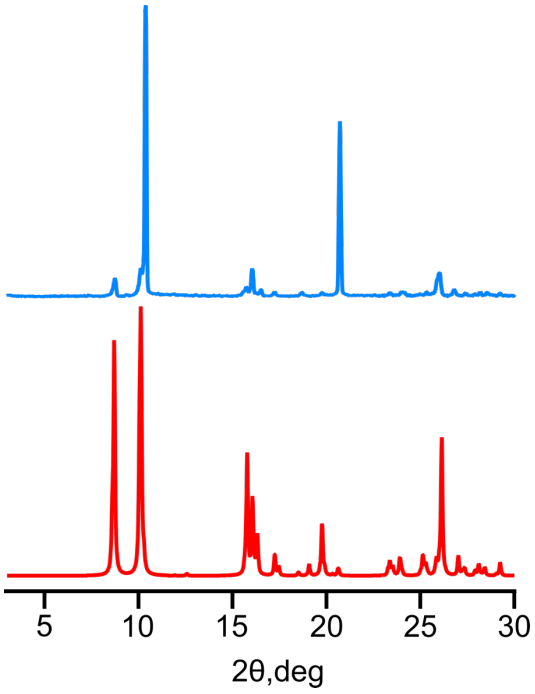

Figure S17. PXRD patterns of $Cu_5(NIP)_4$: simulated (red) and experimental (light blue).

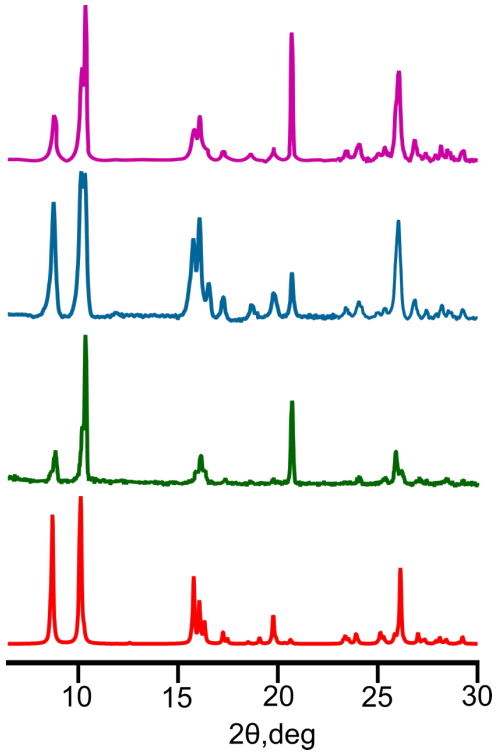

Figure S18. PXRD patterns of simulated $Cu_5(NIP)_4$ (red), experimental $Cu_{4.8}Mn_{0.2}$-NIP (green), experimental $Cu_{4.4}Fe_{0.6}$-NIP (blue), and experimental $Cu_{4.8}Rh_{0.2}$-NIP (pink).

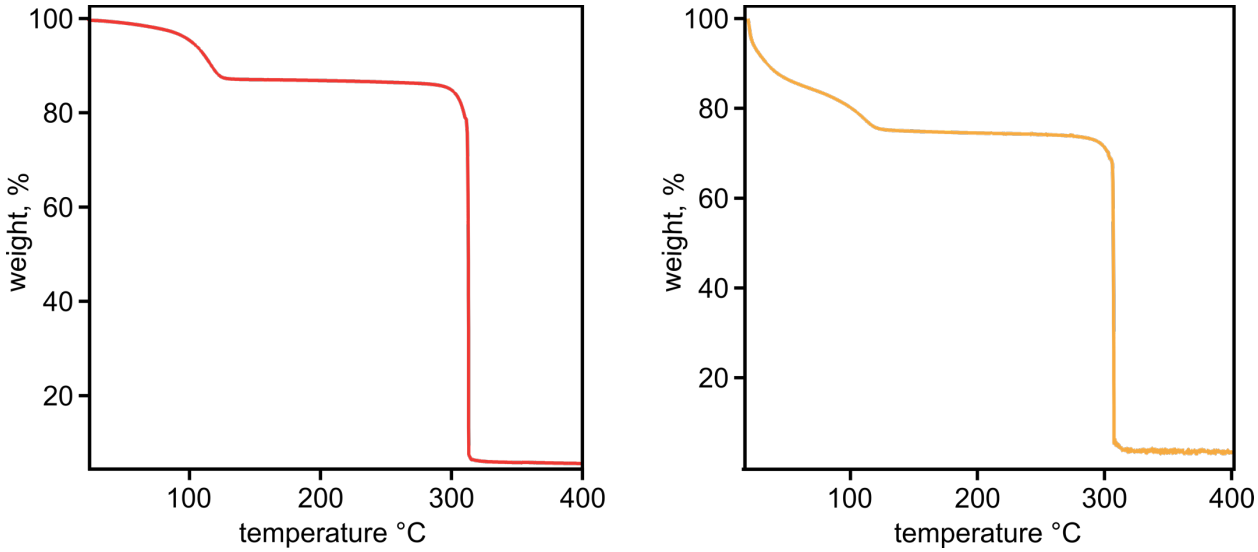

Figure S19. TGA plots of (*left*) $Cu_{4.8}Mn_{0.2}$-NIP and (*right*) $Cu_{4.4}Fe_{0.6}$-NIP.

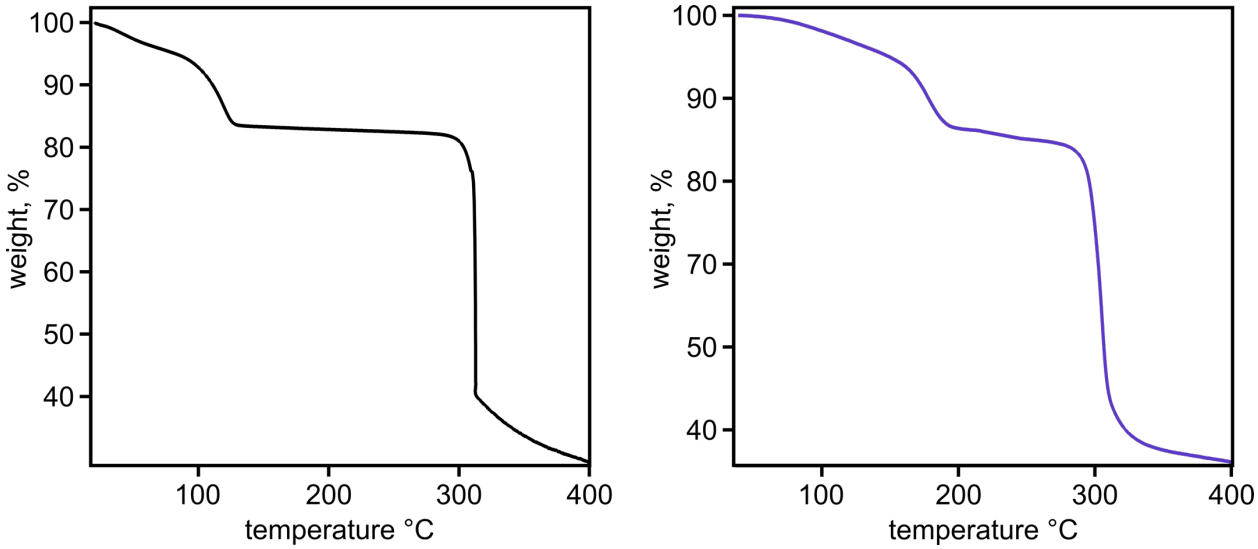

Figure S20. TGA plots of (*left*) $Cu_5(NIP)_4$ and (*right*) $Cu_{4.8}Rh_{0.2}$-NIP.

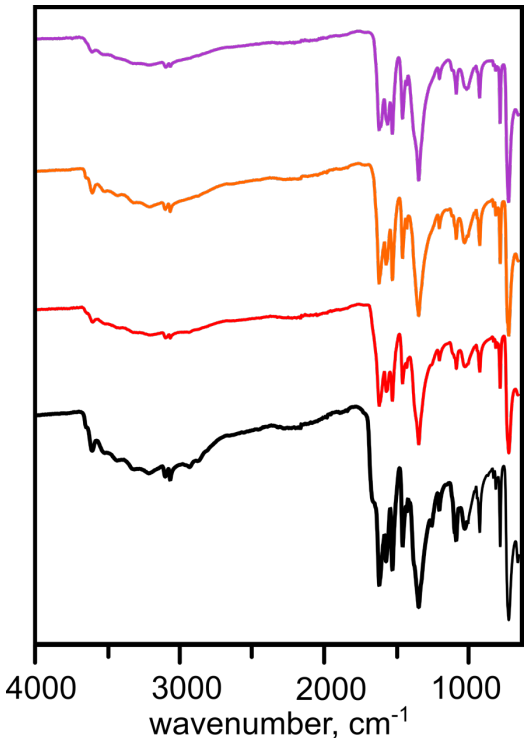

Figure S21. FTIR spectra of $Cu_5(NIP)_4$ (black), $Cu_{4.8}Mn_{0.2}$-NIP (red), $Cu_{4.4}Fe_{0.6}$-NIP (orange), and $Cu_{4.8}Rh_{0.2}$-NIP (purple).

Table S5. Characteristics of metal atomic Voronoi–Dirichlet polyhedra in the structures of monometallic MOFs collected in the temperature range of 293–295 K.

Co_9HHTP_4

atom/atom	*d*(Co···Co), Å	*Ω*(Co···Co), %
Co1/Co2	4.96	0.00

$Cu_3(BTC)_2$

atom/atom	*d*(Cu···Cu), Å	*Ω*(Cu···Cu), %
Cu1/Cu1	2.63	9.46

$Cu_5(NIP)_4$

atom/atom	*d*(Cu···Cu), Å	*Ω*(Cu···Cu), %
Cu1/Cu2	3.20	2.60 (× 2)
Cu2/Cu3	3.32	0.00
Cu1/Cu3	3.50	0.00

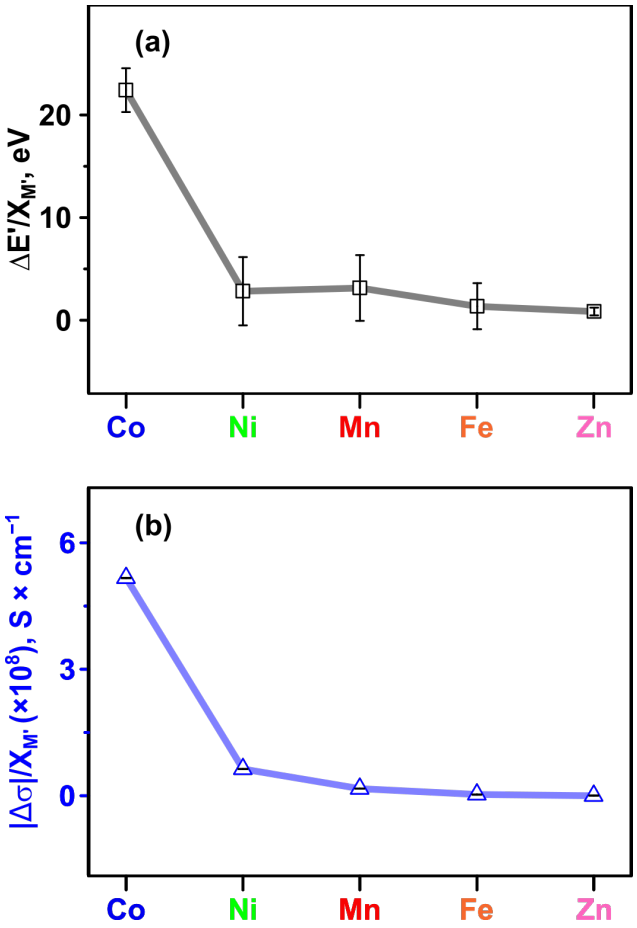

Figure S22. Analysis of $Cu_{3-X}M'_X(BTC)_2$ (M′ = Co, Ni, Mn, Fe, and Zn) as a function of M′ to evaluate (*a*) changes in valence band onset ($\Delta E'/X_{M'}$) and (*b*) changes in conductivity ($|\Delta\sigma|/X_{M'}$). Standard error is depicted by black lines.

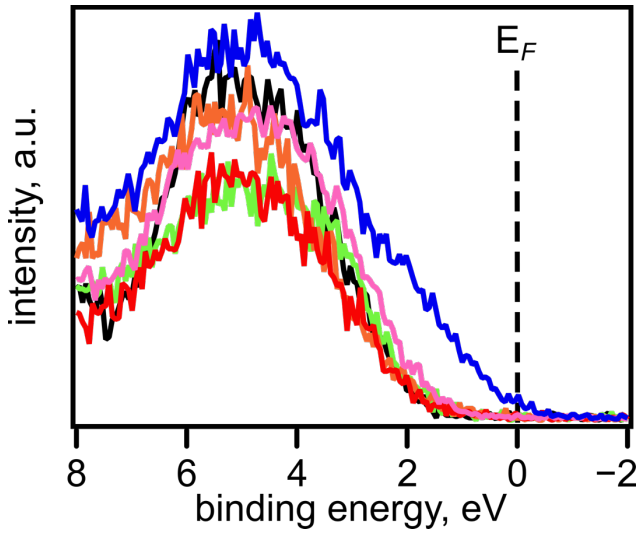

Figure S23. XPS data showing the valence band regions for $Cu_3(BTC)_2$ (black), $Cu_{2.79}Co_{0.21}$-BTC (blue), $Cu_{2.8}Ni_{0.2}$-BTC (green), $Cu_{2.8}Mn_{0.2}$-BTC (red), $Cu_{2.7}Fe_{0.3}$-BTC (orange), and $Cu_{1.6}Zn_{1.4}$-BTC (pink).

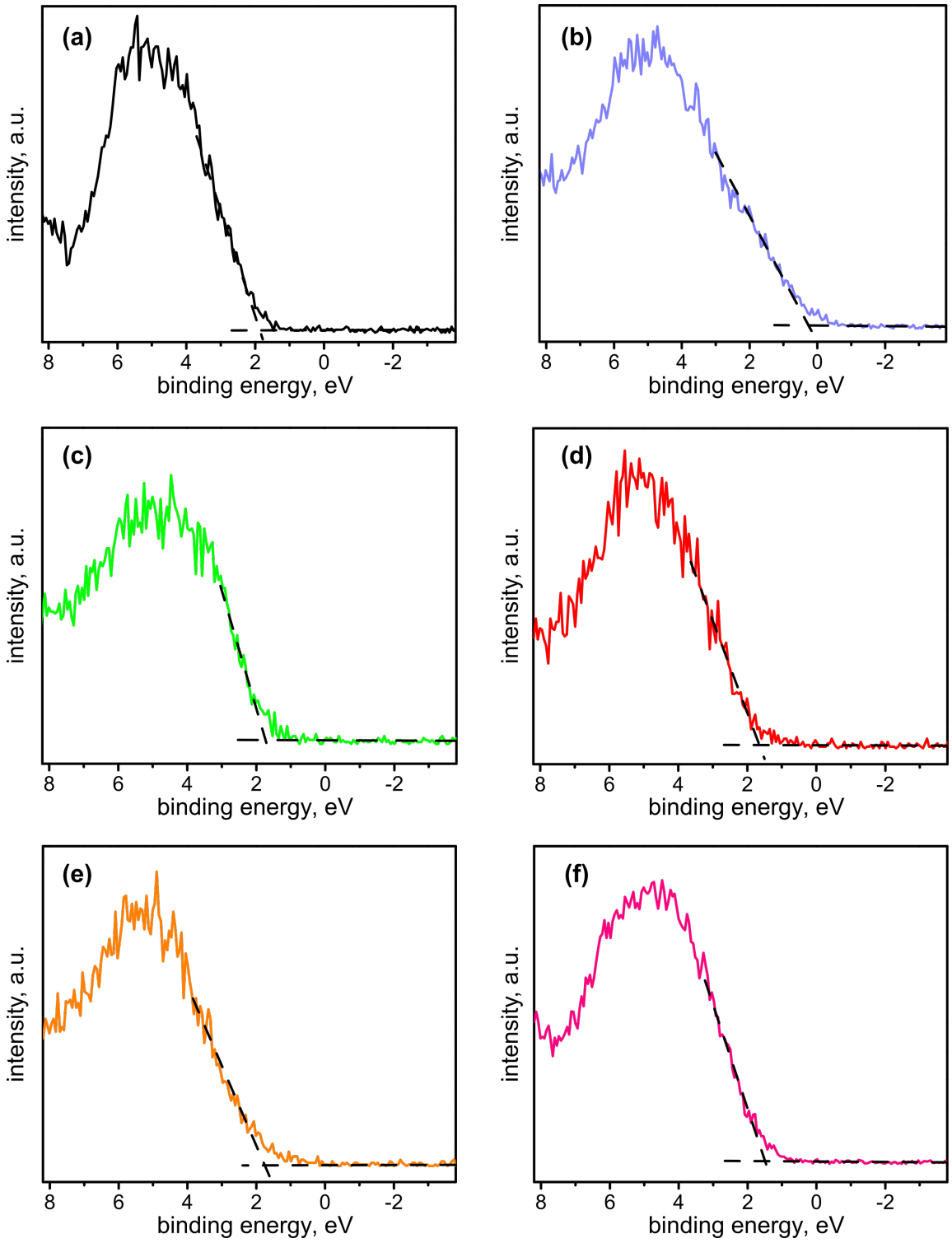

Figure S24. XPS data for the valence band region of (*a*) $Cu_3(BTC)_2$, (*b*) $Cu_{2.79}Co_{0.21}$-BTC, (*c*) $Cu_{2.8}Ni_{0.2}$-BTC, (*d*) $Cu_{2.8}Mn_{0.2}$-BTC, (*e*) $Cu_{2.7}Fe_{0.3}$-BTC, and (*f*) $Cu_{1.6}Zn_{1.4}$-BTC. The valence band onset (*E*′) for each system was calculated from the intersection of the black dashed lines on each spectrum. The valence band onset values for $Cu_{3-X}M'_X(BTC)_2$ can be found in Table S6.

Table S6. Valence band onset results for $Cu_3(BTC)_2$, $Cu_{3-X}M'_X(BTC)_2$ (M′ = Co, Ni, Mn, Fe, and Zn), $Cu_3(HHTP)_2$, $Cu_{3-X}M'_X(HHTP)_2$ (M′ = Co, Mn, Ni, and Rh), $Cu_5(NIP)_4$, and $Cu_{5-X}M'_X(NIP)_4$ M′ = Mn, Fe, and Rh) MOFs.

MOF	valence band onset (eV)	standard error (eV)
$Cu_3(BTC)_2$	1.88	0.150
$Cu_{2.79}Co_{0.21}$-BTC	0.288	0.0200
$Cu_{2.8}Ni_{0.2}$-BTC	1.72	0.116
$Cu_{2.8}Mn_{0.2}$-BTC	1.66	0.167
$Cu_{2.7}Fe_{0.3}$-BTC	1.76	0.136
$Cu_{1.6}Zn_{1.4}$-BTC	1.50	0.0904
$Cu_3(HHTP)_2$	1.51	0.172
$Cu_{2.5}Co_{0.5}$-HHTP	1.20	0.0657
$Cu_{2.0}Mn_{1.0}$-HHTP	1.11	0.0583
$Cu_{1.5}Ni_{1.5}$-HHTP	1.38	0.0835
$Cu_{2.6}Rh_{0.4}$-HHTP	1.51	0.109
$Cu_5(NIP)_4$	1.55	0.0865
$Cu_{4.8}Mn_{0.2}$-NIP	1.73	0.133
$Cu_{4.4}Fe_{0.6}$-NIP	2.04	0.195
$Cu_{4.8}Rh_{0.2}$-NIP	1.49	0.0626

Table S7. Valence band onset (E'), changes in valence band onset compared to $Cu_3(BTC)_2$ ($\Delta E'$), mole fraction of M′ metal ($X_{M'}$), and changes in valence band onset per mole fraction of M′ ($\Delta E'/X_{M'}$) for $Cu_{3-X}M'_X(BTC)_2$ (M′ = Co, Ni, Mn, Fe, and Zn).

MOF	E' (eV)	$\Delta E'^*$ (eV)	$X_{M'}$	$\Delta E'/X_{M'}$ (eV)
$Cu_{2.79}Co_{0.21}$-BTC	0.288	1.59	0.0710	22.4
$Cu_{2.83}Ni_{0.17}$-BTC	1.72	0.161	0.0570	2.82
$Cu_{2.79}Mn_{0.21}$-BTC	1.66	0.219	0.0700	3.12
$Cu_{2.73}Fe_{0.27}$-BTC	1.76	0.121	0.0900	1.34
$Cu_{1.62}Zn_{1.38}$-BTC	1.50	0.381	0.540	0.829

$^*\Delta E' = E'(Cu_3(BTC)_2) - E'(Cu_{3-X}M'_X(BTC)_2)$

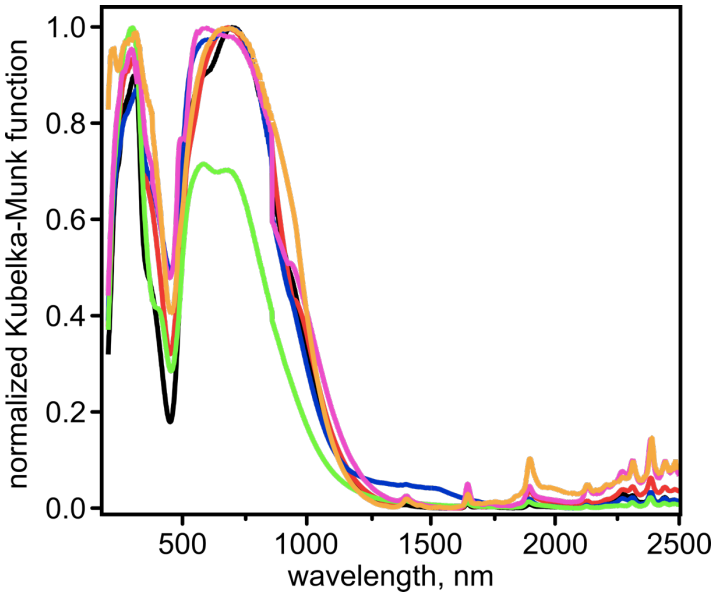

Figure S25. Normalized diffuse reflectance spectra for $Cu_{3-X}M'_X(BTC)_2$ MOFs: $Cu_3(BTC)_2$ (black), $Cu_{2.79}Co_{0.21}$-BTC (dark blue), $Cu_{2.7}Ni_{0.3}$-BTC (light green), $Cu_{2.4}Mn_{0.6}$-BTC (red), $Cu_{2.2}Fe_{0.8}$-BTC (orange), and $Cu_{1.6}Zn_{1.4}$-BTC (dark pink).

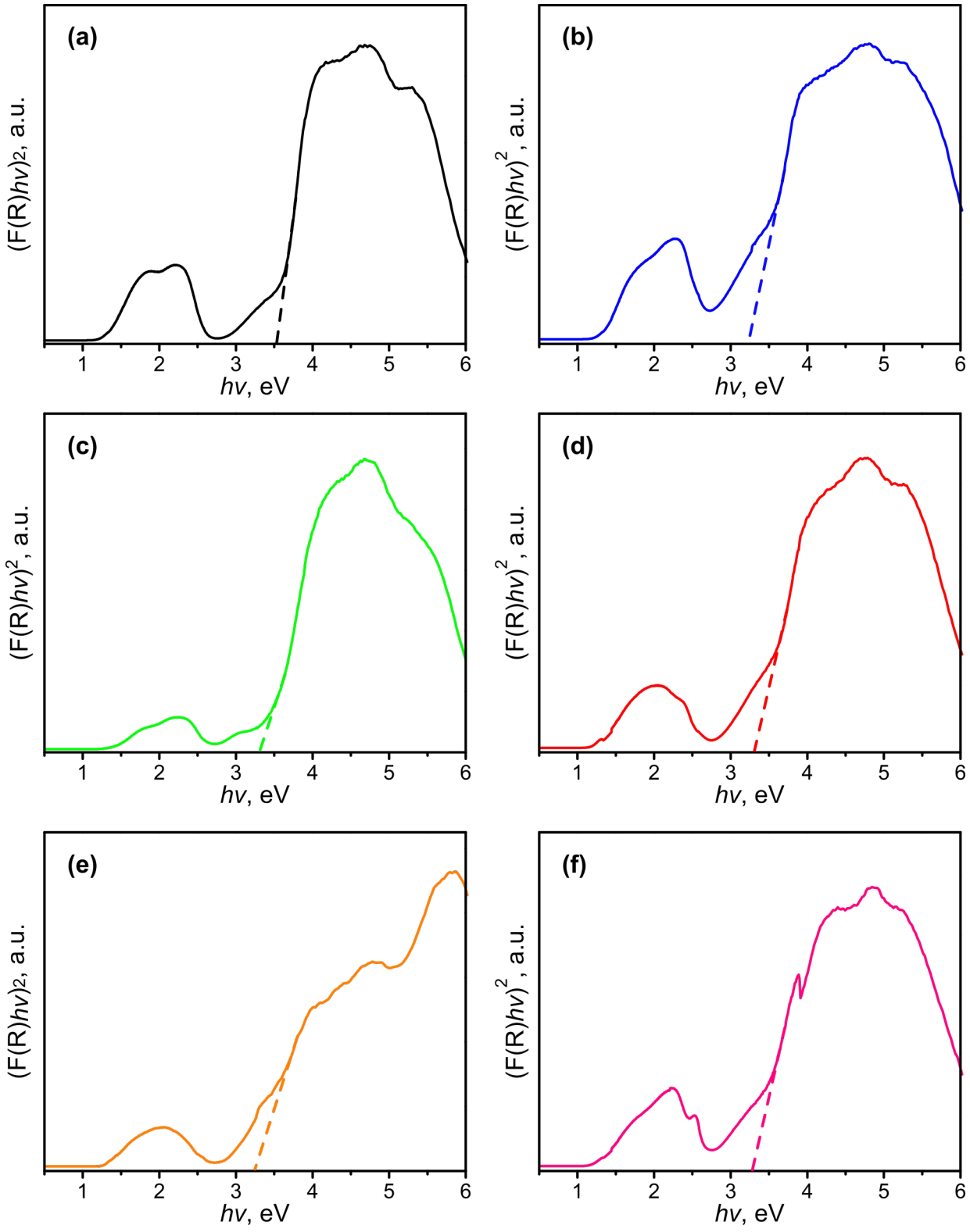

Figure S26. Tauc plots for (*a*) $Cu_3(BTC)_2$, (*b*) $Cu_{2.79}Co_{0.21}$-BTC, (*c*) $Cu_{2.7}Ni_{0.3}$-BTC, (*d*) $Cu_{2.4}Mn_{0.6}$-BTC, (*e*) $Cu_{2.2}Fe_{0.8}$-BTC, and (*f*) $Cu_{1.6}Zn_{1.4}$-BTC. The band gap values for $Cu_{3-X}M'_X(BTC)_2$ can be found in Table S8.

Table S8. Band gap results for $Cu_3(BTC)_2$, $Cu_{3-X}M'_X(BTC)_2$ (M′ = Co, Ni, Mn, Fe, and Zn), $Cu_3(HHTP)_2$, $Cu_{3-X}M'_X(HHTP)_2$ (M′ = Co, Mn, Ni, and Rh), $Cu_5(NIP)_4$ and $Cu_{5-X}M'_X(NIP)_4$ (M′ = Mn, Fe, and Rh) MOFs.

MOF	band gap (eV)	standard error (eV)
$Cu_3(BTC)_2$	3.55	0.143
$Cu_{2.79}Co_{0.21}$-BTC	3.22	0.170
$Cu_{2.7}Ni_{0.3}$-BTC	3.32	0.128
$Cu_{2.4}Mn_{0.6}$-BTC	3.30	0.137
$Cu_{2.2}Fe_{0.8}$-BTC	3.24	0.101
$Cu_{1.6}Zn_{1.4}$-BTC	3.27	0.0890
$Cu_3(HHTP)_2$	0.895	0.00765
$Cu_{2.5}$-HHTP	1.06	0.0109
$Cu_{2.0}Mn_{1.0}$-HHTP	1.17	0.00744
$Cu_{1.5}Ni_{1.5}$-HHTP	1.20	0.00991
$Cu_{2.6}Rh_{0.4}$-HHTP	1.23	0.0160
$Cu_5(NIP)_4$	2.86	0.0314
$Cu_{4.8}Mn_{0.2}$-NIP	2.91	0.0380
$Cu_{4.4}Fe_{0.6}$-NIP	2.76	0.0472
$Cu_{4.8}Rh_{0.2}$-NIP	3.53	0.0365

Table S9. Band gap (E_g), changes in band gap compared to $Cu_3(BTC)_2$ (ΔE_g), mole fraction of M′ metal ($X_{M'}$), and changes in band gap per mole fraction of M′ ($\Delta E_g/X_{M'}$) for $Cu_{3-X}M'_X(BTC)_2$ (M′ = Co, Ni, Mn, Fe, and Zn).

MOF	E_g (eV)	ΔE_g* (eV)	$X_{M'}$	$\Delta E_g/X_{M'}$ (eV)
$Cu_{2.79}Co_{0.21}$-BTC	3.22	0.334	0.0710	4.70
$Cu_{2.66}Ni_{0.34}$-BTC	3.32	0.233	0.113	2.06
$Cu_{2.41}Mn_{0.59}$-BTC	3.30	0.257	0.197	1.30
$Cu_{2.25}Fe_{0.75}$-BTC	3.24	0.310	0.250	1.24
$Cu_{1.62}Zn_{1.38}$-BTC	3.27	0.281	0.540	0.610

*$\Delta E_g = E_g(Cu_3(BTC)_2) - E_g(Cu_{3-X}M'_X(BTC)_2)$

Table S10. Conductivity results for $Cu_3(BTC)_2$, $Cu_{3-X}M'_X(BTC)_2$ (M′ = Co, Ni, Mn, Fe, and Zn), $Cu_3(HHTP)_2$, $Cu_{3-X}M'_X(HHTP)_2$ (M′ = Co, Mn, Ni, and Rh), $Cu_5(NIP)_4$ and $Cu_{5-X}M'_X(NIP)_4$ (M′ = Mn, Fe, and Rh) MOFs.

MOF	conductivity value ($S \times cm^{-1}$)	standard error ($S \times cm^{-1}$)
$Cu_3(BTC)_2$	2.93×10^{-10}	7.83×10^{-13}
$Cu_{2.9}Co_{0.1}$-BTC	8.92×10^{-10}	3.43×10^{-12}
$Cu_{2.82}Co_{0.18}$-BTC	1.42×10^{-9}	4.61×10^{-12}
$Cu_{2.79}Co_{0.21}$-BTC	3.96×10^{-9}	1.86×10^{-12}
$Cu_{2.7}Ni_{0.3}$-BTC	1.01×10^{-9}	5.01×10^{-13}
$Cu_{2.8}Mn_{0.2}$-BTC	3.30×10^{-10}	4.83×10^{-12}
$Cu_{2.6}Mn_{0.4}$-BTC	3.84×10^{-10}	1.23×10^{-12}
$Cu_{2.4}Mn_{0.6}$-BTC	6.24×10^{-10}	8.23×10^{-13}
$Cu_{2.7}Fe_{0.3}$-BTC	3.28×10^{-10}	1.77×10^{-12}
$Cu_{2.6}Fe_{0.4}$-BTC	3.29×10^{-10}	1.22×10^{-12}
$Cu_{2.2}Fe_{0.8}$-BTC	3.63×10^{-10}	2.75×10^{-13}
$Cu_{1.6}Zn_{1.4}$-BTC	3.15×10^{-10}	7.96×10^{-14}
$Cu_3(HHTP)_2$	4.91×10^{-4}	1.60×10^{-6}
$Cu_{2.5}Co_{0.5}$-HHTP	2.05×10^{-5}	1.36×10^{-7}
$Cu_{2.0}Mn_{1.0}$-HHTP	8.77×10^{-6}	8.77×10^{-8}
$Cu_{1.5}Ni_{1.5}$-HHTP	9.91×10^{-8}	6.26×10^{-10}
$Cu_{2.6}Rh_{0.4}$-HHTP	8.62×10^{-9}	3.57×10^{-11}
$Cu_5(NIP)_4$	5.48×10^{-6}	1.43×10^{-8}
$Cu_{4.8}Mn_{0.2}$-NIP	4.25×10^{-6}	1.91×10^{-8}
$Cu_{4.4}Fe_{0.6}$-NIP	1.17×10^{-7}	5.01×10^{-10}
$Cu_{4.8}Rh_{0.2}$-NIP	1.32×10^{-8}	4.34×10^{-10}

Table S11. Conductivity (σ), changes in conductivity compared to $Cu_3(BTC)_2$ ($|\Delta\sigma|$), mole fraction of M′ metal ($X_{M'}$), and changes in conductivity per mole fraction of M′ ($|\Delta\sigma|/X_{M'}$) for $Cu_{3-X}M'_X(BTC)_2$ (M′ = Co, Ni, Mn, Fe, and Zn).

MOF	σ (S × cm^{-1})	$\lvert\Delta\sigma\rvert^*$ (S × cm^{-1})	$X_{M'}$	$\lvert\Delta\sigma\rvert/X_{M'}$ (S × cm^{-1})
$Cu_{2.79}Co_{0.21}$-BTC	3.96×10^{-9}	3.67×10^{-9}	0.0710	5.17×10^{-8}
$Cu_{2.66}Ni_{0.34}$-BTC	1.01×10^{-9}	7.17×10^{-10}	0.113	6.35×10^{-9}
$Cu_{2.41}Mn_{0.59}$-BTC	6.24×10^{-10}	3.31×10^{-10}	0.197	1.68×10^{-9}
$Cu_{2.25}Fe_{0.75}$-BTC	3.63×10^{-10}	7.00×10^{-11}	0.250	2.80×10^{-10}
$Cu_{1.62}Zn_{1.38}$-BTC	3.15×10^{-10}	2.20×10^{-11}	0.540	4.78×10^{-11}

*$|\Delta\sigma| = |\sigma(Cu_{3-X}M'_X(BTC)_2) - \sigma(Cu_3(BTC)_2)|$

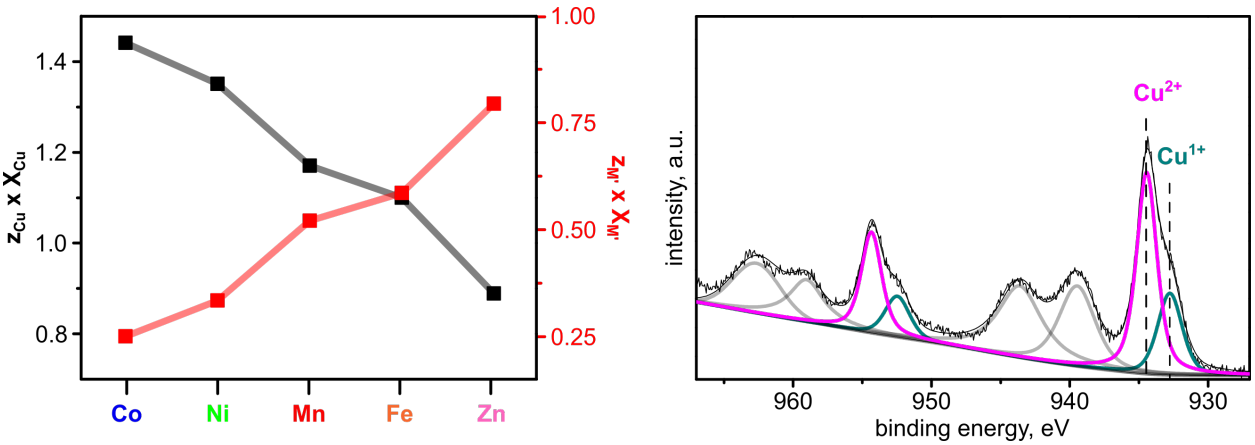

Figure S27. (*left*) The ($z_{Cu} \times X_{Cu}$) and ($z_{M'} \times X_{M'}$) values estimated for $Cu_{3-X}M'_X(BTC)_2$ (M′ = Co, Ni, Mn, Fe, and Zn). (*right*) XPS data for the Cu(2p) region of $Cu_3(BTC)_2$ showing the assigned peaks of Cu^{2+} at 934.7 and Cu^{1+} at 933.0 eV.[2] The percentage of Cu^{2+} and Cu^{1+} for $Cu_{3-X}M'_X(BTC)_2$ can be found in Table S12.

Table S12. Percentage of Cu^{2+} and Cu^{1+} in $Cu_3(BTC)_2$, $Cu_{3-x}M'_x(BTC)_2$ (M′ = Co, Ni, Mn, Fe, and Zn), in $Cu_3(BTC)_2$ and $Cu_{3-x}M'_x(HHTP)_2$ (M′ = Co, Mn, and Ni) MOFs.

MOF	% (Cu^{2+})	% (Cu^{1+})
$Cu_3(BTC)_2$	69.0	31.0
$Cu_{2.79}Co_{0.21}$-BTC	55.0	45.0
$Cu_{2.7}Ni_{0.3}$-BTC	42.6	57.4
$Cu_{2.4}Mn_{0.6}$-BTC	45.6	54.4
$Cu_{2.2}Fe_{0.8}$-BTC	47.2	52.8
$Cu_{1.6}Zn_{1.4}$-BTC	64.9	35.1
$Cu_3(HHTP)_2$	52.5	47.5
$Cu_{2.5}Co_{0.5}$-HHTP	43.5	56.5
$Cu_{2.0}Mn_{1.0}$-HHTP	51.5	48.5
$Cu_{1.5}Ni_{1.5}$-HHTP	56.7	43.3

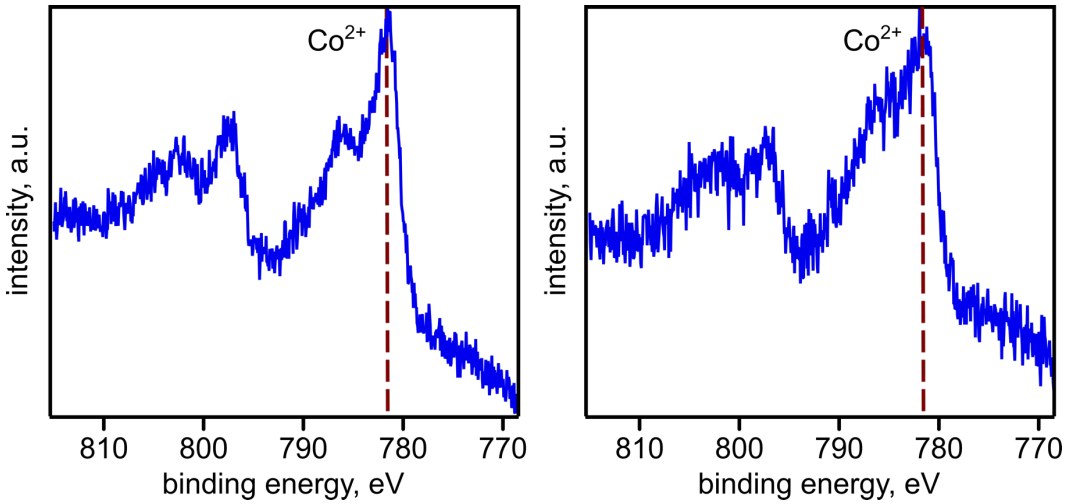

Figure S28. XPS data for the Co(2p) region of (*left*) $Cu_{2.79}Co_{0.21}$-BTC and (*right*) $Cu_{2.5}Co_{0.5}$-HHTP showing the presence of Co in the +2 oxidation state in both binuclear (781.6 eV) and mononuclear (781.3 eV) heterometallic systems. This binding energy is in agreement with what has been previously reported in the literature for $Cu_{3-x}Co_x(BTC)_2$[27] and other Co^{2+} species;[28] and the 16 eV splitting between the $2p_{3/2}$ and $2p_{1/2}$ peaks observed here is also characteristic of Co^{2+}.[29,30] Furthermore, the high binding energy shoulder around 785.9 eV is attributed to a satellite feature that is observed for Co^{2+} but not for Co^{3+}.[29,31,32] The relative intensity of this satellite peak is apparently very sensitive to the exact environment of the Co ion and varies with concentration.

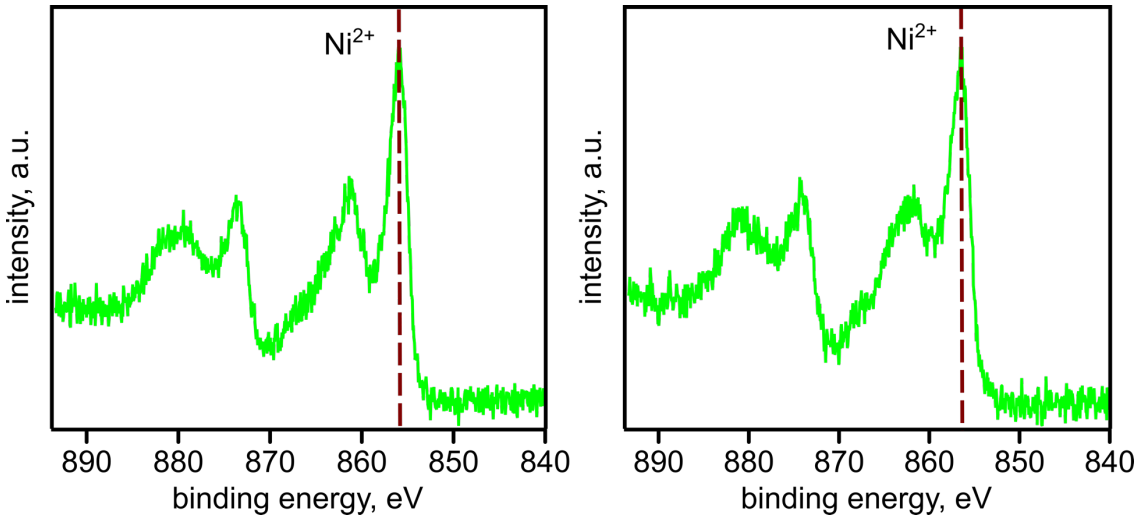

Figure S29. XPS data for the Ni(2p) region of (*left*) $Cu_{2.7}Ni_{0.3}$-BTC and (*right*) $Cu_{1.5}Ni_{1.5}$-HHTP showing the presence of Ni in the +2 oxidation state in both binuclear and mononuclear heterometallic systems based on the Ni($2p_{3/2}$) binding energies at 856.3 eV. Ni(II) chlorides[33] and hydroxides[34] have binding energies of ~856 eV, and the intense shakeup peak at 861.8 eV is also characteristic of Ni^{2+}.[23]

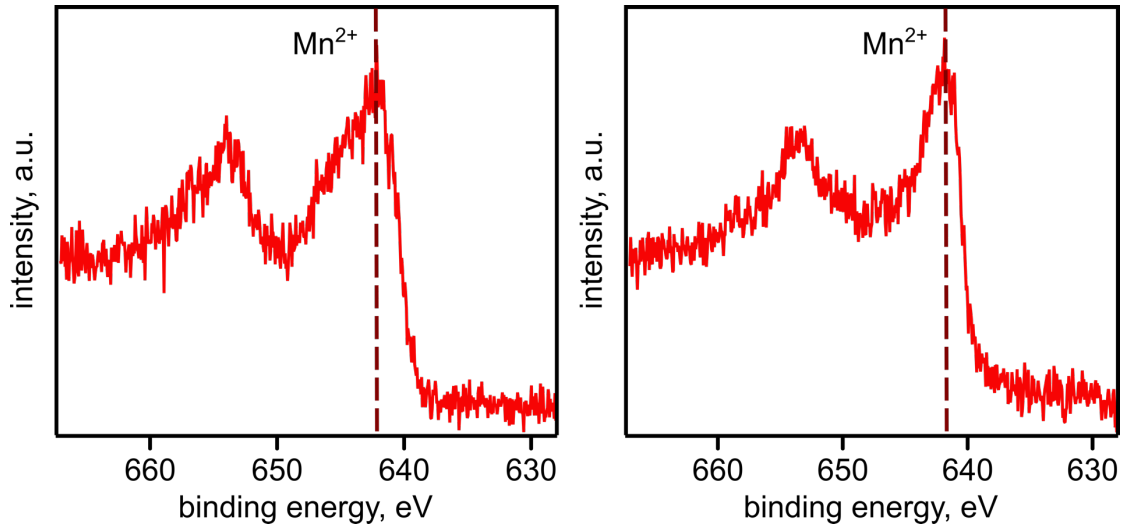

Figure S30. XPS data for the Mn(2p) region of (*left*) $Cu_{2.4}Mn_{0.6}$-BTC and (*right*) $Cu_{2.0}Mn_{1.0}$-HHTP showing the presence of Mn in the +2 oxidation state in both binuclear and mononuclear heterometallic systems. The higher binding energy satellite peak that is associated with Mn^{2+} (~646 eV)[22] is observed for $Cu_{2.4}Mn_{0.6}$-BTC, suggesting that the species at 642.2 eV should be assigned to Mn^{2+} rather than Mn^{4+}, which does not exhibit this satellite feature. [22] Since $Cu_{2.0}Mn_{1.0}$-HHTP has a similar binding energy of 641.8 eV, this species is also attributed to Mn^{2+}. Furthermore, other Mn^{2+} species in the literature such as $MnCl_2$ and $MnBr_2$ have binding energies around 642 eV.[24]

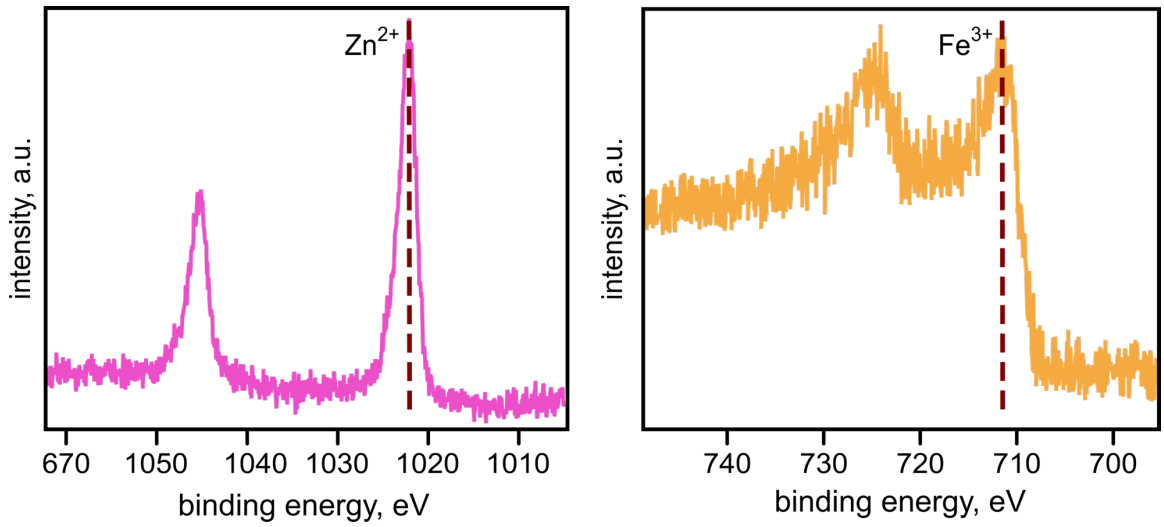

Figure S31. XPS data for (*left*) the Zn(2p) region of $Cu_{1.6}Zn_{1.4}$-BTC and for (*right*) the Fe(2p) region of $Cu_{2.2}Fe_{0.8}$-BTC. The Zn($2p_{3/2}$) peak appears at 1022.4 eV, which is a binding energy consistent with the expected Zn oxidation state of +2.[25,27] The binding energy for Fe($2p_{3/2}$) at 711.3 eV is tentatively assigned to Fe^{3+} as the major species. Binding energies of the metal ions in $Cu_{3-X}M'_X(BTC)_2$ often correspond to those of the metal chlorides, as observed in this work for M′ = Co,[25] Ni and Mn. The binding energy of Fe(III) chloride is similar to $Cu_{2.2}Fe_{0.8}$-BTC at 711.3−711.5 eV, whereas Fe(II) chloride is lower at 709.8−710.8 eV.[24,26]

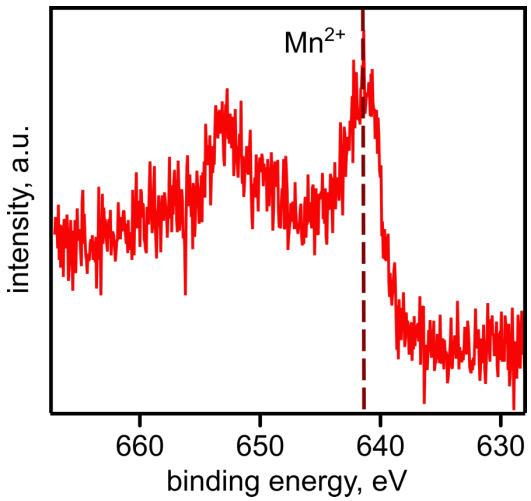

Figure S32. XPS data for the Mn(2p) region of $Cu_{4.8}Mn_{0.2}$-NIP. The Mn($2p_{3/2}$) binding energy of 641. 9 eV suggests a +2 oxidation state, as explained in Figure S30.

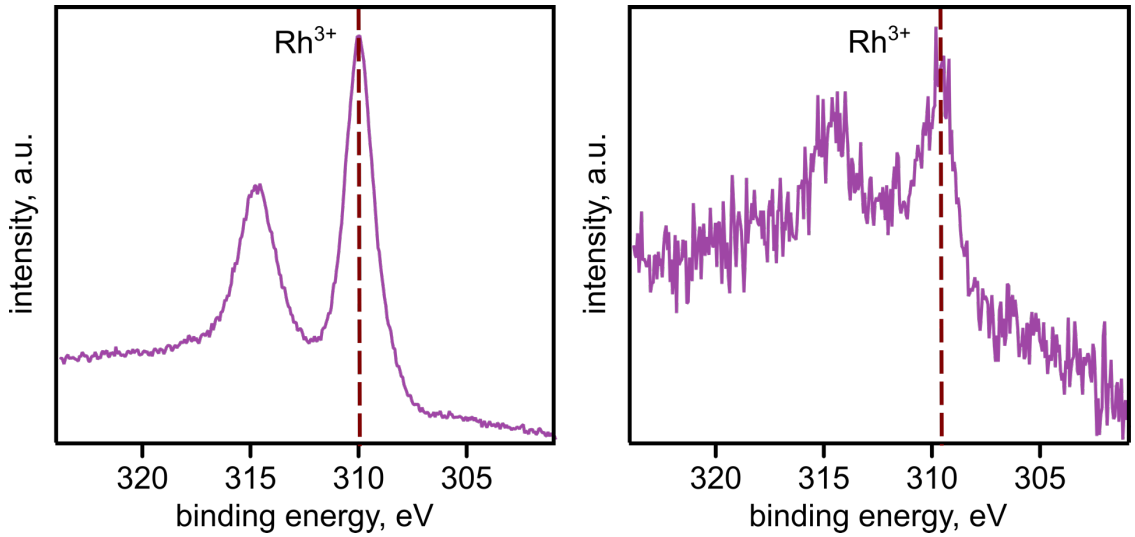

Figure S33. XPS data for the Rh(3d) region of (*left*) $Cu_{2.6}Rh_{0.4}$-HHTP and (*right*) $Cu_{4.8}Rh_{0.2}$-NIP MOFs showing the presence of Rh in the +3 oxidation state. The Rh($3d_{5/2}$) binding energies of 310.0 eV for $Cu_{2.6}Rh_{0.4}$-HHTP and 309.7 eV for $Cu_{4.8}Rh_{0.2}$-NIP are consistent with the ~310 eV value reported in the literature for Rh^{3+}.[20,21]

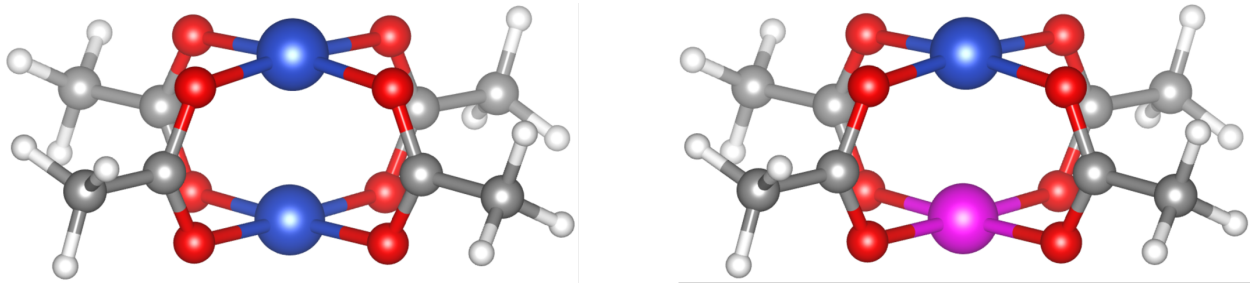

Figure S34. Truncated models of the $Cu_{3-X}M'_X(BTC)_2$ system utilized for DFT calculations: (*left*) $Cu_2(OAc)_4$ and (*right*) $CuM'(OAc)_4$ (where M′ = Mn, Fe, Co, Ni, and Zn). The dark blue, pink, gray, red, and white spheres represent Cu, M′, C, O, and H atoms, respectively.

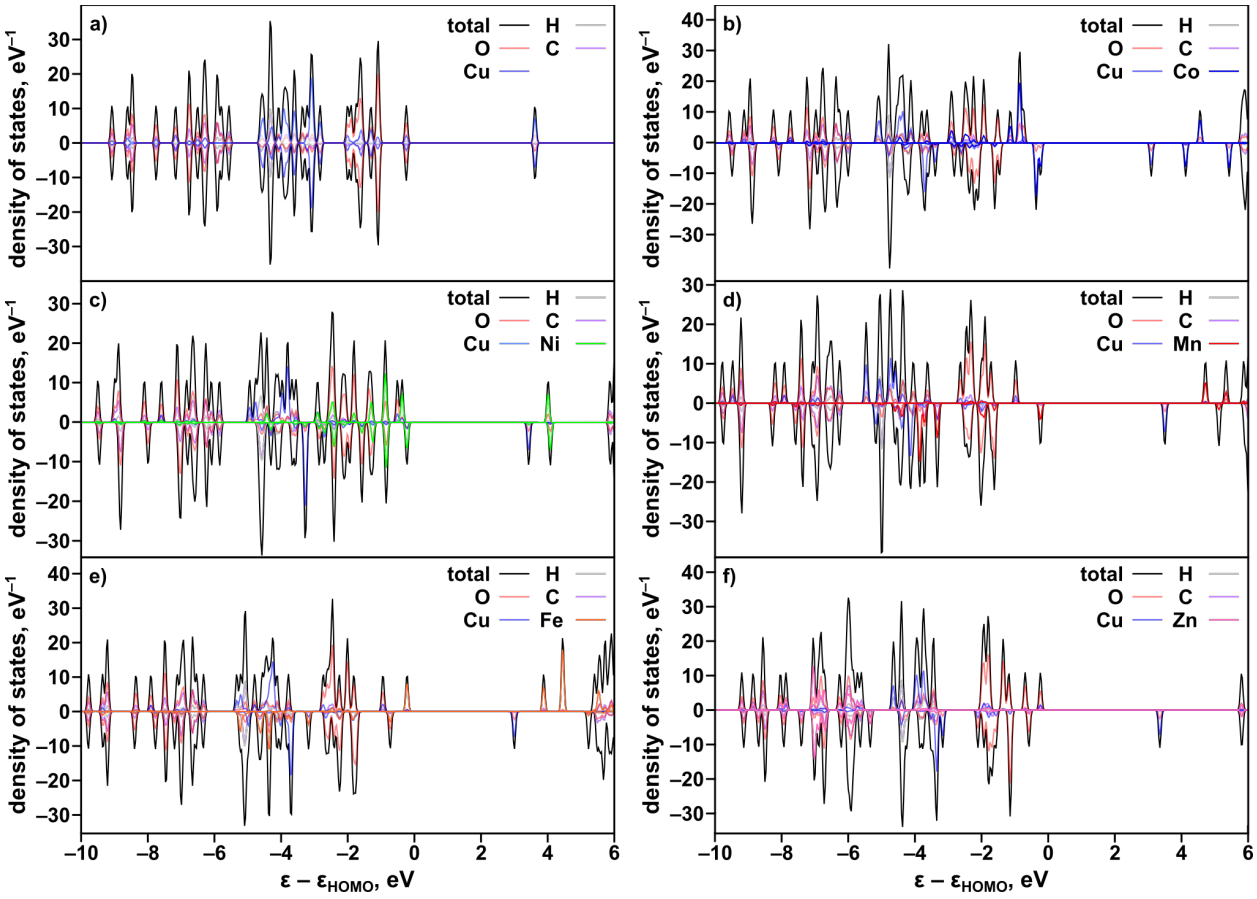

Figure S35. Total and partial DOS of $Cu_{3-X}M'_X(BTC)_2$ systems calculated using optimal geometries of: (*a*) $Cu_2(OAc)_4$ (*b*) $CuCo(OAc)_4$, (*c*) $CuNi(OAc)_4$, (*d*) $CuMn(OAc)_4$, (*e*) $CuFe(OAc)_4$, and (*f*) $CuZn(OAc)_4$.

Table S13. Cu and M′ charge analysis* for Cu/M′ in $Cu_2(OBn)_4$ and $CuM'(OBn)_4$ (M′ = Co, Ni, Mn, Fe and Zn).

model	z_1	z_2	z_3
B3LYP-D3/m6-31G*			
$Cu_2(OBn)_4$	1.58/1.58	1.27/1.28	0.54/0.54
$CuCo(OBn)_4$	0.85/0.82	1.26/1.42	0.51/0.78
$CuNi(OBn)_4$	0.95/1.21	1.19/1.28	0.53/0.68
$CuMn(OBn)_4$	0.84/0.90	1.23/1.55	0.47/1.01
$CuFe(OBn)_4$	0.85/0.78	1.26/1.48	0.45/0.96
$CuZn(OBn)_4$	1.40/2.03	1.24/1.40	0.51/0.89
ωB97X-V/6-31G*			
$Cu_2(OBn)_4$	2.02/2.09	1.23/1.24	0.92/0.91
$CuCo(OBn)_4$	0.64/0.70	1.25/1.38	0.88/1.05
$CuNi(OBn)_4$	0.85/0.91	1.22/1.31	0.91/0.96
$CuMn(OBn)_4$	0.70/1.26	1.24/1.53	0.83/1.25
$CuFe(OBn)_4$	0.66/0.98	1.24/1.46	0.81/1.22
$CuZn(OBn)_4$	2.08/2.36	1.22/1.37	0.91/0.98

Bader (z_1),[72] atomic dipole-corrected-Hishfeld-atomic (z_2),[72] and Mulliken (z_3) charges estimated based on the B3LYP-D3/m6-31G and ωB97X-V/6-31G* methods using the optimized geometry for the $CuM'(OBn)_4$ cluster.

Table S14. Lowest electron excitations, TDDFT 'corrected' HOMO–LUMO gap, and corresponding electron transition for $Cu_2(OBn)_4$ and $CuM'(OBn)_4$ (M′ = Co, Ni, Mn, Fe, and Zn) of the optimized geometries.*

model	lowest electron excitation, eV	transition
$Cu_2(OBn)_4$ triplet	1.83	MMCT**
$CuCo(OBn)_4$ quintet	0.20	MLCT
$CuNi(OBn)_4$ quartet	0.22	LMCT
$CuMn(OBn)_4$ quintet (LS)	0.40	MLCT
$CuMn(OBn)_4$ septet (HS)	1.88	LMCT
$CuFe(OBn)_4$ sextet	0.77	MLCT
$CuZn(OBn)_4$ doublet	1.91	LMCT

* Geometry optimization was performed with B3LYP-D3/m6-31G* level of theory and electron excitations were calculated with ω-B97X-V/6-31G* level of theory.
** metal-to-metal charge transfer

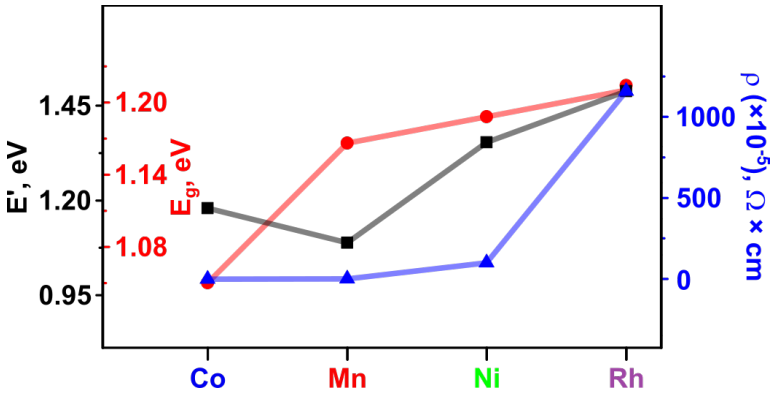

Figure S36. Analysis of $Cu_{3-X}M'_X(HHTP)_2$ (M′ = Co, Ni, Mn, and Rh) as a function of M′ to evaluate (*a*) valence band onset (*E*′), (*b*) resistivity (ρ), and (*c*) optical bad gap (E_g).

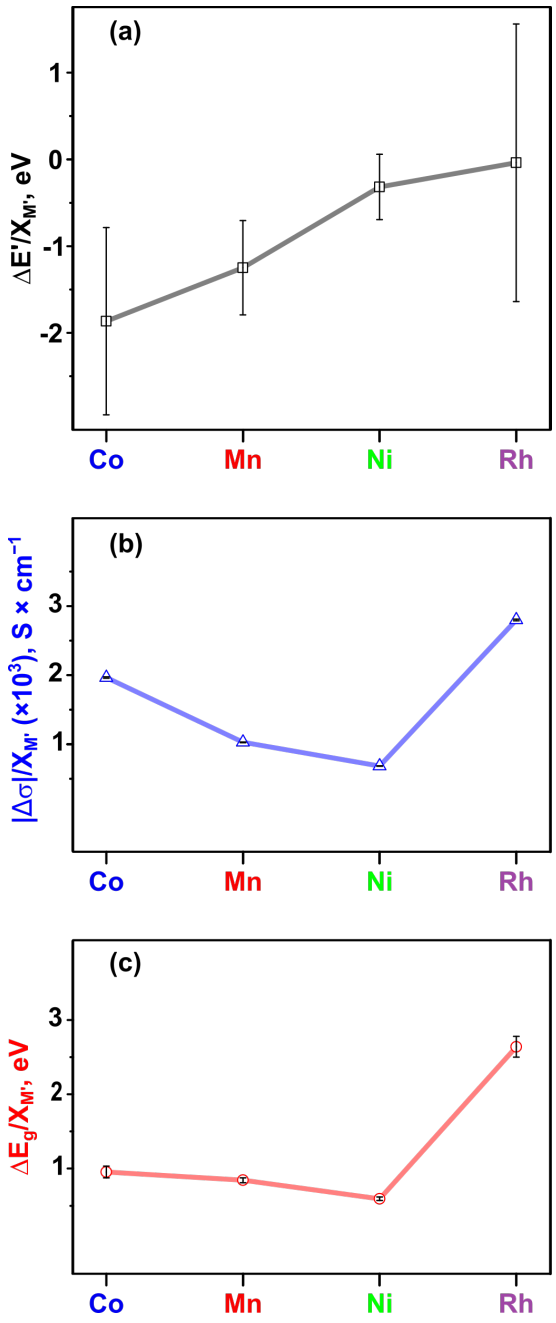

Figure S37. Analysis of $Cu_{3-x}M'_x(HHTP)_2$ (M′ = Co, Ni, Mn, and Rh) as a function of M′ to evaluate (*a*) changes in valence band onset ($\Delta E'/X_{M'}$), (*b*) changes in conductivity ($|\Delta\sigma|/X_{M'}$), and (*c*) changes in optical bad gap ($\Delta E_g/X_{M'}$). Standard error is depicted by black lines.

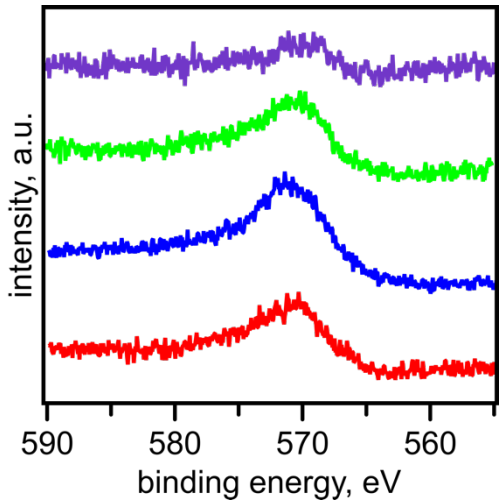

Figure S38. XPS data for the Cu(LMM) region of $Cu_{2.0}Mn_{1.0}$-HHTP (red), $Cu_{2.5}Co_{0.5}$-HHTP (dark blue), $Cu_{1.5}Ni_{1.5}$-HHTP (light green), and $Cu_{2.6}Rh_{0.4}$-HHTP (purple), showing the broad peak indicative of oxidized Cu ions rather than metallic Cu[49].

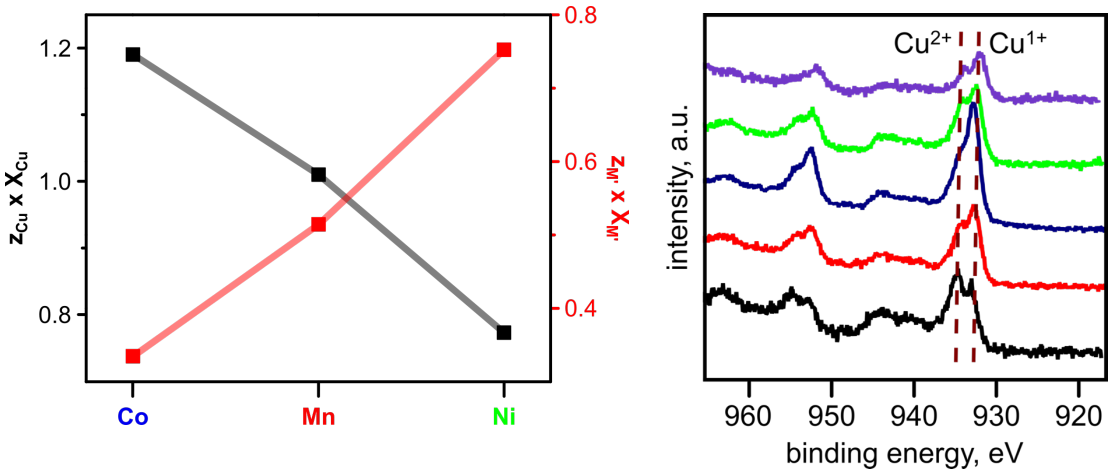

Figure S39. (*left*) The ($z_{Cu} \times X_{Cu}$) and ($z_{M'} \times X_{M'}$) values estimated for $Cu_{3-X}M'_X(HHTP)_2$ (M′ = Co, Mn, and Ni). (*right*) XPS data for the Cu(2p) regions of $Cu_3(HHTP)_2$ (black), $Cu_{2.0}Mn_{1.0}$-HHTP (red), $Cu_{2.5}Co_{0.5}$-HHTP (dark blue), $Cu_{15}Ni_{1.5}$-HHTP (light green), and $Cu_{2.6}Rh_{0.4}$-HHTP (purple) showing the assigned peaks of Cu^{2+} at 934.7 and Cu^{1+} at 933.0 eV[2]. The percentage of Cu^{2+} and Cu^{1+} for $Cu_{3-X}M'_X(HHTP)_2$ can be found in Table S12.

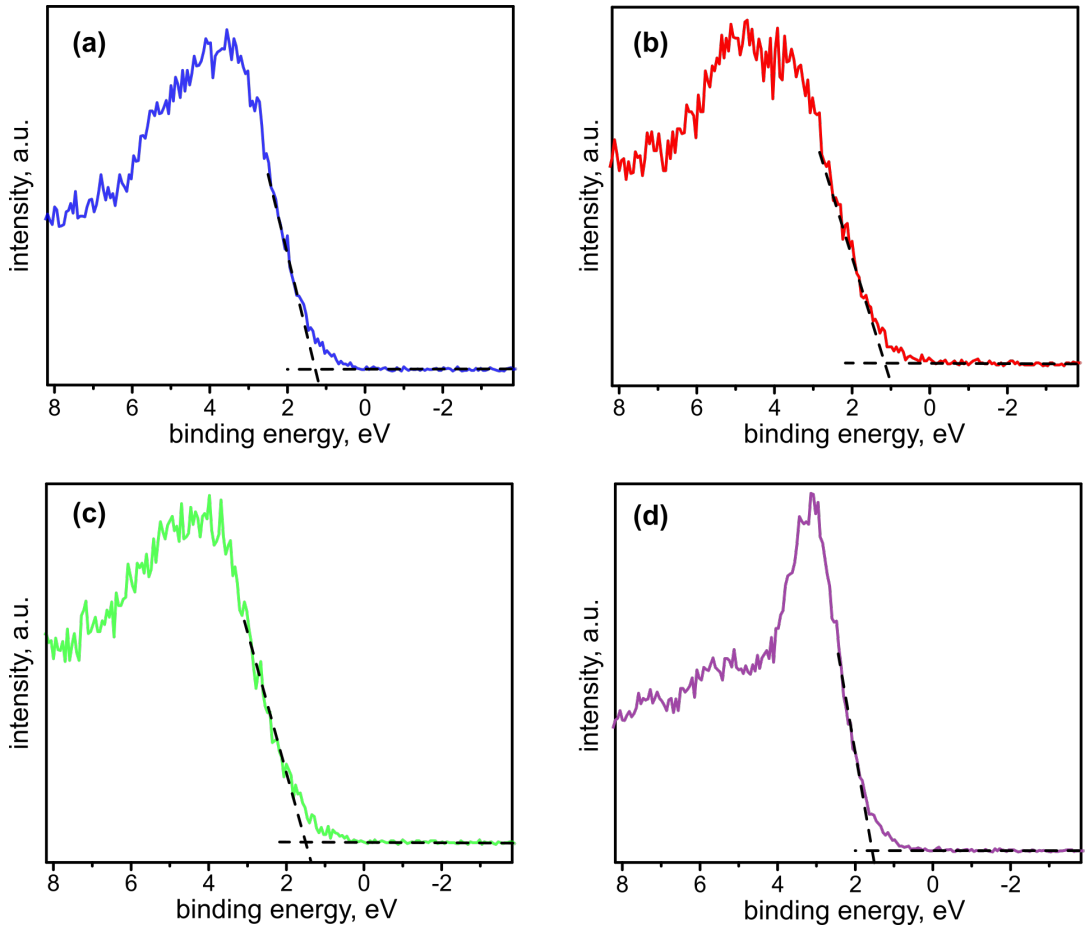

Figure S40. XPS data for the valence band region of (*a*) $Cu_{2.5}Co_{0.5}$-HHTP, (*b*) $Cu_{2.0}Mn_{1.0}$-HHTP, (*c*) $Cu_{1.5}Ni_{1.5}$-HHTP, and (*d*) $Cu_{2.6}Rh_{0.4}$-HHTP. The valence band onset (E') for each system was calculated from the intersection of the black dashed lines on each spectrum. The valence band onset values for $Cu_{3-X}M'_X(HHTP)_2$ can be found in Table S6.

Table S15. Valence band onset (E'), changes in valence band onset compared to $Cu_3(HHTP)_2$ ($\Delta E'$), mole fraction of M′ metal ($X_{M'}$), and changes in valence band onset per mole fraction of M′ ($\Delta E'/X_{M'}$) for $Cu_{3-X}M'_X(HHTP)_2$ (M′ = Co, Mn, Ni, and Rh).

MOF	E' (eV)	$\Delta E'^*$ (eV)	$X_{M'}$	$\Delta E'/X_{M'}$ (eV)
$Cu_{2.5}Co_{0.5}$-HHTP	1.20	-0.308	0.170	-1.81
$Cu_{2.0}Mn_{1.0}$-HHTP	1.11	-0.398	0.333	-1.20
$Cu_{1.5}Ni_{1.5}$-HHTP	1.38	-0.133	0.506	-0.263
$Cu_{2.6}Rh_{0.4}$-HHTP	1.51	0.002	0.126	0.016

$^*\Delta E' = E'(Cu_{3-X}M'_X(HHTP)_2) - E'(Cu_3(HHTP)_2)$

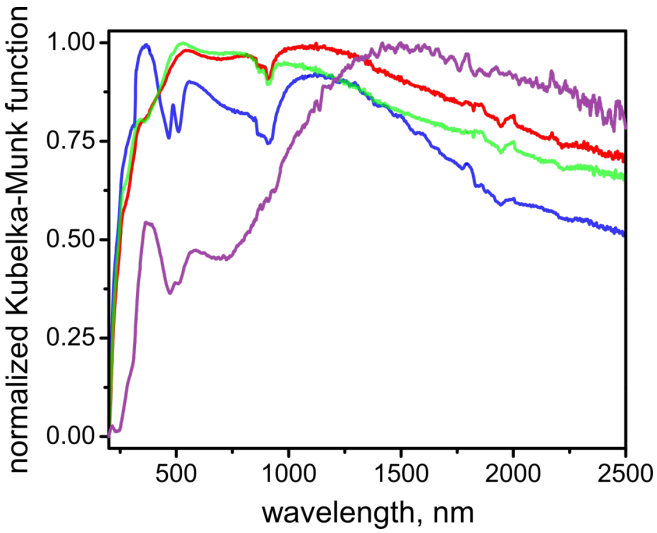

Figure S41. Normalized diffuse reflectance spectra for $Cu_{2.5}Co_{0.5}$-HHTP (dark blue), $Cu_{2.0}Mn_{1.0}$-HHTP (red), $Cu_{1.5}Ni_{1.5}$-HHTP (light green), and $Cu_{2.6}Rh_{0.4}$-HHTP (purple).

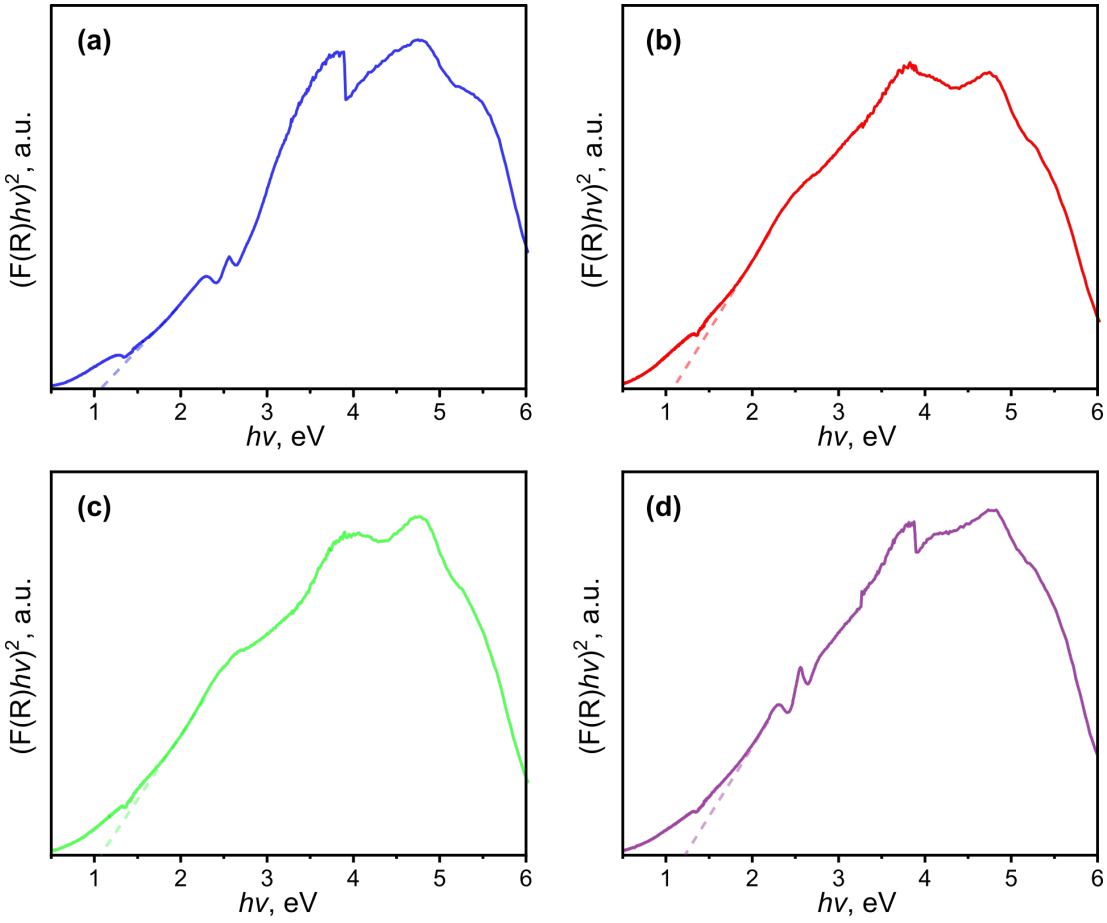

Figure S42. Tauc plots for (*a*) $Cu_{2.5}Co_{0.5}$-HHTP, (*b*) $Cu_{2.0}Mn_{1.0}$-HHTP, (*c*) $Cu_{1.5}Ni_{1.5}$-HHTP, and (*d*) $Cu_{2.6}Rh_{0.4}$-HHTP. The band gap values for $Cu_{3-X}M'_X(HHTP)_2$ can be found in Table S8.

Table S16. Band gap (E_g), changes in band gap compared to $Cu_3(HHTP)_2$ (ΔE_g), mole fraction of M′ metal ($X_{M'}$), and changes in band gap per mole fraction of M′ ($E_g/X_{M'}$) for $Cu_{3-X}M'_X(HHTP)_2$ (M′ = Co, Mn, Ni, and Rh).

MOF	E_g (eV)	ΔE_g* (eV)	$X_{M'}$	$\Delta E_g/X_{M'}$ (eV)
$Cu_{2.5}Co_{0.5}$-HHTP	1.06	0.162	0.170	0.956
$Cu_{2.0}Mn_{1.0}$-HHTP	1.17	0.278	0.333	0.843
$Cu_{1.5}Ni_{1.5}$-HHTP	1.20	0.301	0.506	0.594
$Cu_{2.6}Rh_{0.4}$-HHTP	1.23	0.333	0.126	2.64

*$\Delta E_g = E_g(Cu_{3-X}M'_X(HHTP)_2) - E_g(Cu_3(HHTP)_2)$

Table S17. Conductivity (σ), changes in conductivity compared to $Cu_3(HHTP)_2$ ($|\Delta\sigma|$), mole fraction of M′ metal ($X_{M'}$), and changes in conductivity per mole fraction of M′ ($|\Delta\sigma|/X_{M'}$) for $Cu_{3-X}M'_X(HHTP)_2$ (M′ = Co, Mn, Ni, and Rh).

MOF	σ (S × cm^{-1})	$\lvert\Delta\sigma\rvert$* (S × cm^{-1})	$X_{M'}$	$\lvert\Delta\sigma\rvert/X_{M'}$ (S × cm^{-1})
$Cu_{2.5}Co_{0.5}$-HHTP	2.05×10^{-5}	4.71×10^{-4}	0.170	2.77×10^{-3}
$Cu_{2.0}Mn_{1.0}$-HHTP	8.77×10^{-6}	4.82×10^{-4}	0.333	1.45×10^{-3}
$Cu_{1.5}Ni_{1.5}$-HHTP	9.91×10^{-8}	4.91×10^{-4}	0.506	9.68×10^{-4}
$Cu_{2.6}Rh_{0.4}$-HHTP	8.62×10^{-9}	4.91×10^{-4}	0.126	3.87×10^{-3}

*$|\Delta\sigma| = |\sigma(Cu_3(HHTP)_2) - \sigma(Cu_{3-X}M'_X(HHTP)_2)|$

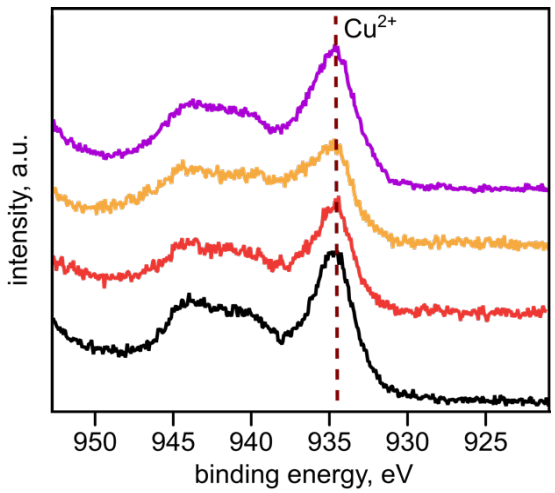

Figure S43. XPS data for the Cu(2p) region of $Cu_5(NIP)_4$ (black), $Cu_{4.8}Mn_{0.2}$-NIP (red), $Cu_{4.4}Fe_{0.6}$-NIP (orange), $Cu_{4.8}Rh_{0.2}$-NIP (purple) showing the presence of Cu primarily in the +2 oxidation state (934.7 eV).[2]

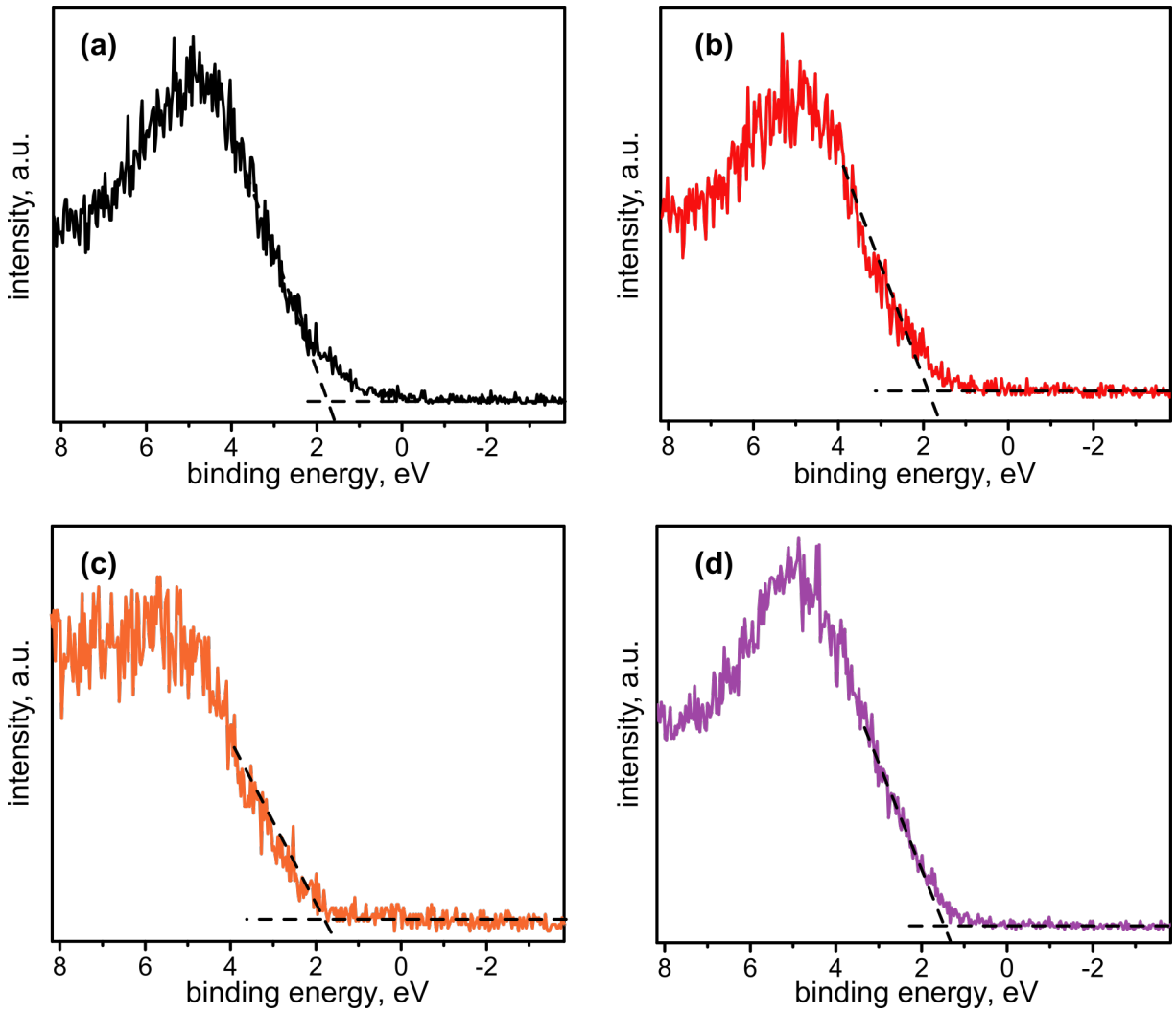

Figure S44. (*left*) XPS data for the valence band region of (*a*) $Cu_5(NIP)_4$, (*b*) $Cu_{4.8}Mn_{0.2}$-NIP, *(c)* $Cu_{4.4}Fe_{0.6}$-NIP, and (*d*) $Cu_{4.8}Rh_{0.2}$-NIP (purple).

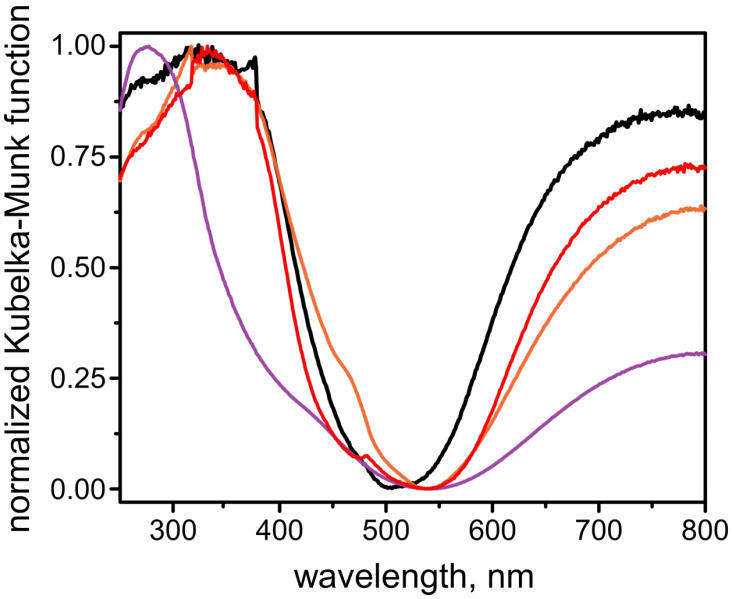

Figure S45. Normalized diffuse reflectance spectra for $Cu_5(NIP)_4$ (black), $Cu_{4.8}Mn_{0.2}$-NIP (red), $Cu_{4.4}Fe_{0.6}$-NIP (orange), and $Cu_{4.8}Rh_{0.2}$-NIP (purple).

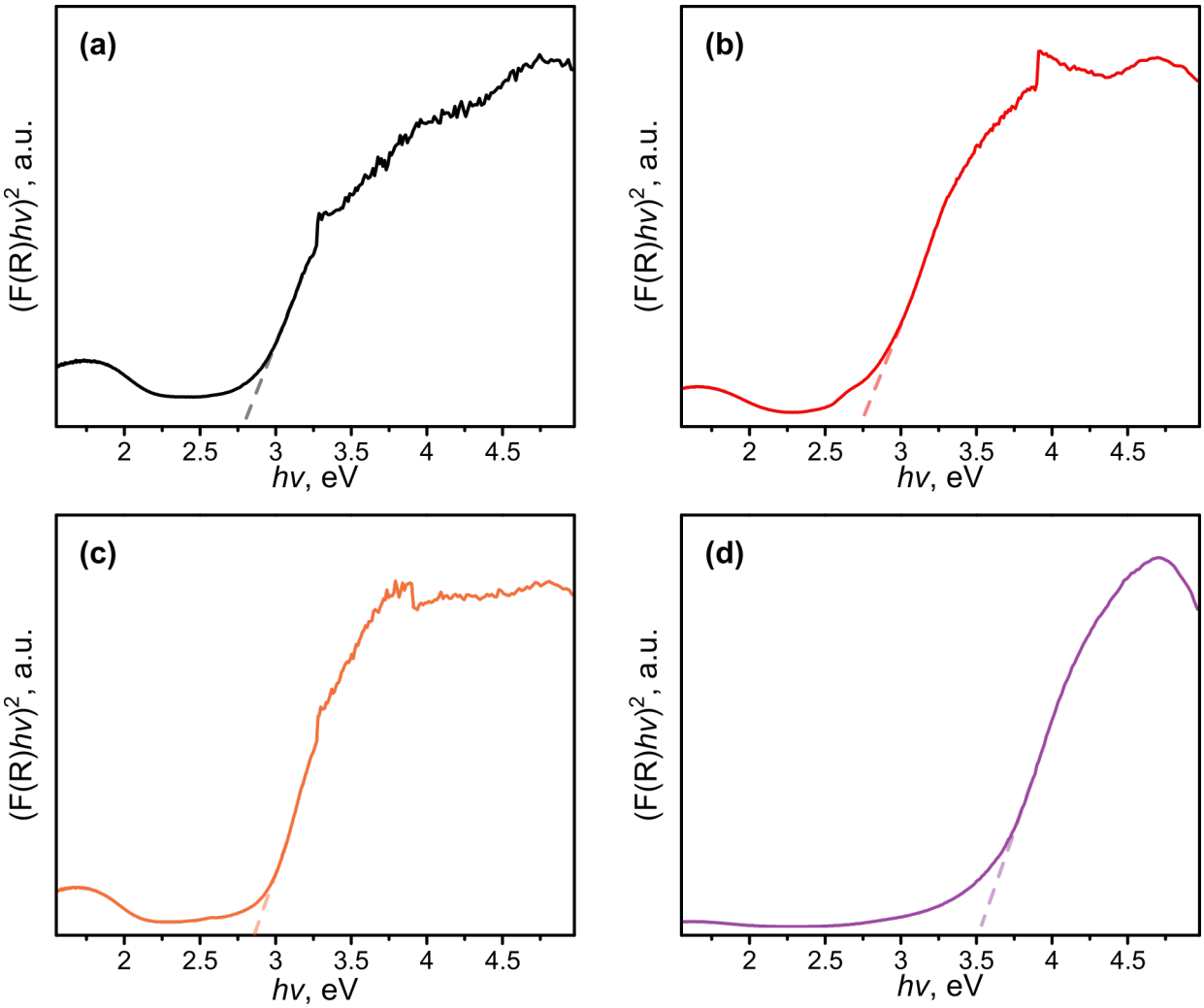

Figure S46. Tauc plots for (*a*) $Cu_5(NIP)_4$, (*b*) $Cu_{4.8}Mn_{0.2}$-NIP, (*c*) $Cu_{4.4}Fe_{0.6}$-NIP, and (*d*) $Cu_{4.8}Rh_{0.2}$-NIP. The band gap values for $Cu_{5-X}M'_X(NIP)_4$ can be found in Table S8.

Table S18. Conductivity (σ), changes in conductivity compared to $Cu_5(NIP)_4$ ($|\Delta\sigma|$), mole fraction of M′ metal ($X_{M'}$), and changes in conductivity per mole fraction of M′ ($|\Delta\sigma|/X_{M'}$) for $Cu_{5-X}M'_X(NIP)_4$ (M′ = Mn, Fe, and Rh).

MOF	σ (S × cm^{-1})	$\lvert\Delta\sigma\rvert^*$ (S × cm^{-1})	$X_{M'}$	$\lvert\Delta\sigma\rvert/X_{M'}$ (S × cm^{-1})
$Cu_{4.8}Mn_{0.2}$-NIP	4.25×10^{-6}	1.23×10^{-6}	0.036	3.42×10^{-5}
$Cu_{4.4}Fe_{0.6}$-NIP	1.17×10^{-7}	5.36×10^{-6}	0.12	4.47×10^{-5}
$Cu_{4.8}Rh_{0.2}$-NIP	1.32×10^{-8}	5.47×10^{-6}	0.036	1.52×10^{-4}

$^*|\Delta\sigma| = |\sigma(Cu_5(NIP)_4) - \sigma(Cu_{5-X}M'_X(NIP)_4)|$

References:

1 S. S.-Y. Chui, S. M.-F. Lo, J. P. H. Charmant, A. G. Orpen and I. D. Williams, *Science*, 1999, **283**, 1148–1150.

2 A. S. Duke, E. A. Dolgopolova, R. P. Galhenage, S. C. Ammal, A. Heyden, M. D. Smith, D. A. Chen and N. B. Shustova, *J. Phys. Chem. C*, 2015, **119**, 27457–27466.

3 Y. Zhao, M. Padmanabhan, Q. Gong, N. Tsumori, Q. Xu and J. Li, *Chem. Commun.*, 2011, **47**, 6377–6379.

4 M. Hmadeh, Z. Lu, Z. Liu, F. Gándara, H. Furukawa, S. Wan, V. Augustyn, R. Chang, L. Liao, F. Zhou, E. Perre, V. Ozolins, K. Suenaga, X. Duan, B. Dunn, Y. Yamamto, O. Terasaki and O. M. Yaghi, *Chem. Mater.*, 2012, **24**, 3511–3513.

5 2016, Bruker AXS, Inc., Madison, Wisconsin, USA.

6 L. Krause, R. Herbst-Irmer, G. M. Sheldrick and D. Stalke, *J. Appl. Crystallogr.*, 2015, **48**, 3–10.

7 G. M. Sheldrick, *Acta Crystallogr. Sect. C, Struct. Chem.*, 2015, **71**, 3–8.

8 G. M. Sheldrick, *Acta Crystallogr. Sect. A Found. Crystallogr.*, 2008, **64**, 112–122.

9 O. V. Dolomanov, L. J. Bourhis, R. J. Gildea, J. A. K. Howard and H. Puschmann, *J. Appl. Crystallogr.*, 2009, **42**, 339–341.

10 A. L. Spek, *Acta Crystallogr. Sect. C Struct. Chem.*, 2015, **71**, 9–18.

11 V. A. Blatov, A. P. Shevchenko and V. N. Serezhkin, *J. Appl. Crystallogr.*, 2000, **33**, 1193.

12 V. A. Blatov, A. P. Shevchenko and D. M. Proserpio, *Cryst. Growth Des.*, 2014, **14**, 3576–3586.

13 E. V. Alexandrov, V. A. Blatov, A. V. Kochetkov and D. M. Proserpio, *CrystEngComm*, 2011, **13**, 3947–3958.

14 P. Swift, *Surf. Interface Anal.*, 1982, **4**, 47–51.

15 T. L. Barr and S. Seal, *J. Vac. Sci. Technol. A Vacuum, Surfaces, Film.*, 1995, **13**, 1239–1246.

16 Y. Dou, T. Fishlock, R. G. Egdell, D. S. L. Law and G. Beamson, *Phys. Rev. B*, 1997, **55**, R13381–R13384.

17 G. Deroubaix and P. Marcus, *Surf. Interface Anal.*, 1992, **18**, 39–46.

18 E. Antonides, E. C. Janse and G. A. Sawatzky, *Phys. Rev. B*, 1977, **15**, 1669–1679.

19 J. Ghijsen, L. H. Tjeng, J. Van Elp, H. Eskes, J. Westerink, G. A. Sawatzky and M. T. Czyzyk, *Phys. Rev. B*, 1988, **38**, 11322–11330.

20 D. M. Shakya, O. A. Ejegbavwo, T. Rajeshkumar, S. D. Senanayake, A. J. Brandt, S. Farzandh, N. Acharya, A. M. Ebrahim, A. I. Frenkel, N. Rui, G. L. Tate, J. R. Monnier, K. D. Vogiatzis, N. B. Shustova and D. A. Chen, *Angew. Chemie - Int. Ed.*, 2019, **58**, 16533–16537.

21 R. Lang, T. Li, D. Matsumura, S. Miao, Y. Ren, Y. T. Cui, Y. Tan, B. Qiao, L. Li, A. Wang, X. Wang and T. Zhang, *Angew. Chemie - Int. Ed.*, 2016, **55**, 16054–16058.

22 E. S. Ilton, J. E. Post, P. J. Heaney, F. T. Ling and S. N. Kerisit, *Appl. Surf. Sci.*, 2016, **366**, 475–485.

23 K. S. Kim, W. E. Baitinger, J. W. Amy and N. Winograd, *J. Electron Spectros. Relat. Phenomena*, 1974, **5**, 351–367.

24 J. C. Carver, G. K. Schweitzer and T. A. Carlson, *J. Chem. Phys.*, 1972, **57**, 973–982.

25 C.D. Wagner, W.M. Riggs, L.E. Davis, J.F. Moulder, *Handbook of X-ray Photoelectron Spectroscopy*, Eden Prairie, MN, Perkin Elmer Corporation, 1979.

26 A. P. Grosvenor, B. A. Kobe, M. C. Biesinger and N. S. McIntyre, *Surf. Interface Anal.*, 2004, **36**, 1564–1574.
27 E. A. Dolgopolova, A. J. Brandt, O. A. Ejegbavwo, A. S. Duke, T. D. Maddumapatabandi, R. P. Galhenage, B. W. Larson, O. G. Reid, S. C. Ammal, A. Heyden, M. Chandrashekhar, V. Stavila, D. A. Chen and N. B. Shustova, *J. Am. Chem. Soc.*, 2017, **139**, 5201–5209.
28 Y. Chen and L. Hu, *J. Solid State Chem.*, 2016, **239**, 23–29.
29 D. C. Frost, C. A. McDowell and I. S. Woolsey, *Chem. Phys. Lett.*, 1972, **17**, 320–323.
30 H. Haraguchi, K. Fujiwara and K. Fuwa, *Chem. Lett.*, 1975, **4**, 409–414.
31 D. J. Cole-Hamilton, *Science*, 2003, **299**, 1702–1706.
32 S. L. T. Andersson and R. F. Howe, *J. Phys. Chem.*, 1989, **93**, 4913–4920.
33 J. Matienzo, L. I. Yin, S. O. Grim and W. E. Swartz, *Inorg. Chem.*, 1973, **12**, 2762–2769.
34 C. P. Li, A. Proctor and D. M. Hercules, *Appl. Spectrosc.*, 1984, **38**, 880–886.
35 D. B. Rorabacher, *Anal. Chem.*, 1991, **63**, 139–146.
36 R. F. Hirsch, *Anal. Chem.*, 1977, **49**, 691A-700A.
37 H.-S. Oh, *Biometrics*, 2013, **69**, 1087–1087.
38 M. Krzywinski and N. Altman, *Nat. Methods*, 2013, **10**, 1041–1042.
39 V. E. Johnson, *Proc. Natl. Acad. Sci.*, 2013, **110**, 19313–19317.
40 C. K. Lin, D. Zhao, W. Y. Gao, Z. Yang, J. Ye, T. Xu, Q. Ge, S. Ma and D. J. Liu, *Inorg. Chem.*, 2012, **51**, 9039–9044.
41 O. A. Ejegbavwo, C. R. Martin, O. A. Olorunfemi, G. A. Leith, R. T. Ly, A. M. Rice, E. A. Dolgopolova, M. D. Smith, S. G. Karakalos, N. Birkner, B. A. Powell, S. Pandey, R. J. Koch, S. T. Misture, H. C. Zur Loye, S. R. Phillpot, K. S. Brinkman and N. B. Shustova, *J. Am. Chem. Soc.*, 2019, **141**, 11628–11640.
42 G. Kresse and J. Hafner, *Phys. Rev. B*, 1993, **47**, 558–561.
43 G. Kresse and J. Furthmüller, *Phys. Rev. B - Condens. Matter Mater. Phys.*, 1996, **54**, 11169–11186.
44 P. E. Blöchl, *Phys. Rev. B*, 1994, **50**, 17953–17979.
45 D. Joubert, *Phys. Rev. B - Condens. Matter Mater. Phys.*, 1999, **59**, 1758–1775.
46 J. P. Perdew, K. Burke and M. Ernzerhof, *Phys. Rev. Lett.*, 1996, **77**, 3865–3868.
47 S. Grimme, J. Antony, S. Ehrlich and H. Krieg, *J. Chem. Phys.*, 2010, **132**, 154104–154122.
48 S. L. Dudarev, G. A. Botton, S. Y. Savrasov, C. J. Humphreys and A. P. Sutton, *Phys. Rev. B*, 1998, **57**, 1505–1509.
49 M. Sieberer, J. Redinger and P. Mohn, *Phys. Rev. B - Condens. Matter Mater. Phys.*, 2007, **75**, 035203.
50 D. M. Bylander, L. Kleinman and S. Lee, *Phys. Rev. B*, 1990, **42**, 1394–1403.
51 M. P. Teter, M. C. Payne and D. C. Allan, *Phys. Rev. B*, 1989, **40**, 12255–12263.
52 J. Heyd and G. E. Scuseria, *J. Chem. Phys.*, 2004, **121**, 1187–1192.
53 A. V. Krukau, O. A. Vydrov, A. F. Izmaylov and G. E. Scuseria, *J. Chem. Phys.*, 2006, **125**, 224106.
54 X. Hai, J. Tahir-Kheli and W. A. Goddard, *J. Phys. Chem. Lett.*, 2011, **2**, 212–217.
55 V. Tripkovic, H. A. Hansen, J. M. Garcia-Lastra and T. Vegge, *J. Phys. Chem. C*, 2018, **122**, 1135–1147.
56 Y. Shao, Z. Gan, E. Epifanovsky, A. T. B. Gilbert, M. Wormit, J. Kussmann, A. W. Lange, A. Behn, J. Deng, X. Feng, D. Ghosh, M. Goldey, P. R. Horn, L. D. Jacobson, I.

Kaliman, R. Z. Khaliullin, T. Kuś, A. Landau, J. Liu, E. I. Proynov, Y. M. Rhee, R. M. Richard, M. A. Rohrdanz, R. P. Steele, E. J. Sundstrom, H. L. Woodcock, P. M. Zimmerman, D. Zuev, B. Albrecht, E. Alguire, B. Austin, G. J. O. Beran, Y. A. Bernard, E. Berquist, K. Brandhorst, K. B. Bravaya, S. T. Brown, D. Casanova, C.-M. Chang, Y. Chen, S. H. Chien, K. D. Closser, D. L. Crittenden, M. Diedenhofen, R. A. DiStasio, H. Do, A. D. Dutoi, R. G. Edgar, S. Fatehi, L. Fusti-Molnar, A. Ghysels, A. Golubeva-Zadorozhnaya, J. Gomes, M. W. D. Hanson-Heine, P. H. P. Harbach, A. W. Hauser, E. G. Hohenstein, Z. C. Holden, T.-C. Jagau, H. Ji, B. Kaduk, K. Khistyaev, J. Kim, J. Kim, R. A. King, P. Klunzinger, D. Kosenkov, T. Kowalczyk, C. M. Krauter, K. U. Lao, A. D. Laurent, K. V. Lawler, S. V. Levchenko, C. Y. Lin, F. Liu, E. Livshits, R. C. Lochan, A. Luenser, P. Manohar, S. F. Manzer, S.-P. Mao, N. Mardirossian, A. V. Marenich, S. A. Maurer, N. J. Mayhall, E. Neuscamman, C. M. Oana, R. Olivares-Amaya, D. P. O'Neill, J. A. Parkhill, T. M. Perrine, R. Peverati, A. Prociuk, D. R. Rehn, E. Rosta, N. J. Russ, S. M. Sharada, S. Sharma, D. W. Small, A. Sodt, T. Stein, D. Stück, Y.-C. Su, A. J. W. Thom, T. Tsuchimochi, V. Vanovschi, L. Vogt, O. Vydrov, T. Wang, M. A. Watson, J. Wenzel, A. White, C. F. Williams, J. Yang, S. Yeganeh, S. R. Yost, Z.-Q. You, I. Y. Zhang, X. Zhang, Y. Zhao, B. R. Brooks, G. K. L. Chan, D. M. Chipman, C. J. Cramer, W. A. Goddard, M. S. Gordon, W. J. Hehre, A. Klamt, H. F. Schaefer, M. W. Schmidt, C. D. Sherrill, D. G. Truhlar, A. Warshel, X. Xu, A. Aspuru-Guzik, R. Baer, A. T. Bell, N. A. Besley, J.-D. Chai, A. Dreuw, B. D. Dunietz, T. R. Furlani, S. R. Gwaltney, C.-P. Hsu, Y. Jung, J. Kong, D. S. Lambrecht, W. Liang, C. Ochsenfeld, V. A. Rassolov, L. V. Slipchenko, J. E. Subotnik, T. Van Voorhis, J. M. Herbert, A. I. Krylov, P. M. W. Gill and M. Head-Gordon, *Mol. Phys.*, 2015, **113**, 184–215.

57 Y. Shao, L. F. Molnar, Y. Jung, J. Kussmann, C. Ochsenfeld, S. T. Brown, A. T. B. Gilbert, L. V. Slipchenko, S. V. Levchenko, D. P. O'Neill, R. A. DiStasio Jr, R. C. Lochan, T. Wang, G. J. O. Beran, N. A. Besley, J. M. Herbert, C. Yeh Lin, T. Van Voorhis, S. Hung Chien, A. Sodt, R. P. Steele, V. A. Rassolov, P. E. Maslen, P. P. Korambath, R. D. Adamson, B. Austin, J. Baker, E. F. C. Byrd, H. Dachsel, R. J. Doerksen, A. Dreuw, B. D. Dunietz, A. D. Dutoi, T. R. Furlani, S. R. Gwaltney, A. Heyden, S. Hirata, C.-P. Hsu, G. Kedziora, R. Z. Khalliulin, P. Klunzinger, A. M. Lee, M. S. Lee, W. Liang, I. Lotan, N. Nair, B. Peters, E. I. Proynov, P. A. Pieniazek, Y. Min Rhee, J. Ritchie, E. Rosta, C. David Sherrill, A. C. Simmonett, J. E. Subotnik, H. Lee Woodcock III, W. Zhang, A. T. Bell, A. K. Chakraborty, D. M. Chipman, F. J. Keil, A. Warshel, W. J. Hehre, H. F. Schaefer III, J. Kong, A. I. Krylov, P. M. W. Gill and M. Head-Gordon, *Phys. Chem. Chem. Phys.*, 2006, **8**, 3172–3191.

58 W. Kohn and L. J. Sham, *Phys. Rev.*, 1965, **140**, A1133–A1138.

59 C. Lee, W. Yang and R. G. Parr, *Phys. Rev. B*, 1988, **37**, 785–789.

60 A. D. Becke, *J. Chem. Phys.*, 1993, **98**, 5648–5652.

61 N. Mardirossian and M. Head-Gordon, *Phys. Chem. Chem. Phys.*, 2014, **16**, 9904.

62 A. V. Mitin, J. Baker and P. Pulay, *J. Chem. Phys.*, 2003, **118**, 7775–7782.

63 S. Grimme, J. Antony, S. Ehrlich and H. Krieg, *J. Chem. Phys.*, 2010, **132**, 154104.

64 K. Burke, J. Werschnik and E. K. U. Gross, *J. Chem. Phys.*, 2005, **123**, 062206.

65 S. Hirata and M. Head-Gordon, *Chem. Phys. Lett.*, 1999, **314**, 291–299.

66 K.-B. Cho, S. Shaik and W. Nam, *J. Phys. Chem. Lett.*, 2012, **3**, 2851–2856.

67 S. O. Odoh, C. J. Cramer, D. G. Truhlar and L. Gagliardi, *Chem. Rev.*, 2015, **115**, 6051–

6111.
68 T. Yanai, D. P. Tew and N. C. Handy, *Chem. Phys. Lett.*, 2004, **393**, 51–57.
69 M. A. Rohrdanz, K. M. Martins and J. M. Herbert, *J. Chem. Phys.*, 2009, **130**, 054112.
70 Y. Wang, X. Jin, H. S. Yu, D. G. Truhlar and X. He, *Proc. Natl. Acad. Sci.*, 2017, **114**, 8487–8492.
71 A. de Oliveira, G. F. de Lima and H. A. De Abreu, *Chem. Phys. Lett.*, 2018, **691**, 283–290.
72 T. Lu and F. Chen, *J. Comput. Chem.*, 2012, **33**, 580–592.